
Article:
Pardikar, K., Capindale, J., Pitt, K. et al. (3 more authors) (2025) Spherical agglomeration for local control of electrode microstructure: Generation of structured agglomerates. Powder Technology, 454. 120688. ISSN 0032-5910

https://doi.org/10.1016/j.powtec.2025.120688

Spherical Agglomeration for Local Control of Electrode Microstructure: Generation of Structured Agglomerates.

*Kunal Pardikar,[1,2] Jediah Capindale,[1,2] Kate Pitt,[1] Igyaar Abdi-Rahman, [1] Denis Cumming,[1,2] Rachel Smith[1,2]**

[1]Department of Chemical and Biological Engineering, The University of Sheffield, Sheffield, S10 2TN, UK
[2]The Faraday Institution, Quad One, Harwell Science and Innovation Campus, Didcot, OX11 0RA, UK
** Corresponding author: rachel.smith@sheffield.ac.uk*

Abstract

In this work, the particle engineering technique Spherical Agglomeration is applied to Li-ion battery materials for the first time. This method involves the generation of structured agglomerates with great potential to act as building blocks of the electrode microstructure, providing control of electrode microstructure and homogeneity of component within the electrode. Process-property relationships are investigated by assessing the impact of varying operating parameters and material properties on agglomerate attributes. The ability to generate a variety of structured agglomerates is demonstrated for both carbon black agglomerates and co-agglomerates of active material and carbon black. These findings reveal that an optimal range of process parameters exists for obtaining spherical co-/agglomerates with good yield. Predictions of co-/agglomerate size are made using a previously published mathematical model, and good qualitative agreement between model and experiment is found, however the model consistently under-predicts co-/agglomerate size.

Keywords

Li-ion battery, Electrode microstructure, Spherical agglomeration, Particle engineering.

1. Introduction

Due to high energy and power density, the long cycle life rechargeable lithium ion battery is one of the most popular forms of energy storage device [1,2]. Electrodes are comprised of active material for de/intercalation of lithium ions, conductive additive for creating fast electronic pathways, and polymer binder for providing structural integrity. There is a vast sphere of research surrounding the active material chemistry, various conductive additives, and component proportions in electrode microstructure with the aim of improving capacity, energy density, and cycle life whilst maintaining safety [3,4].

The manufacturing process chain for electrodes plays a key role in the quality and function of the electrode, however in comparison to active material synthesis it is a relatively understudied area of investigation. It is well known that the conventional electrode manufacturing steps of mixing of particulate components to formulate the slurry, casting of the slurry on to current collector, and drying for solvent removal can generate undesired heterogeneity in the electrode microstructure [5–7].

A variety of issues affect the distribution of individual components in the finished dry electrode, including inadequate dispersion of particulate materials in the viscous slurry, segregation of components during the mixing step, sedimentation of large particles during the casting step, and carbon black/binder migration during drying [8–10]. These effects can lead to a poorly distributed and heterogeneous electrode.

The heterogeneity induced through spatial variability of the active material and conductive additive distribution can lead to differences in local resistances. Heterogeneity does not only refer to the respective ratios of components within a specific area, but also the active material particle size and distribution of carbon additive aggregates. These factors directly affect the tortuosity and conductivity network of the electrode microstructure [11].

Advanced manufacturing techniques are being employed in electrode production such as spray drying [12–14], electrostatic spray deposition (ESD) [15–17] and templating in various forms [18–20]. The motivation behind these technologies is to enable local control over the electrode microstructure and prevent poor distribution of components. Local control over the electrode microstructure is desirable for the design of electrodes with suitable microstructure for specific applications and requirements. For example, a highly porous microstructure is desired for improving high C-rate performance of thick electrodes, whereas, a less porous microstructure is desired for improving energy density of thin electrodes. High C-rate performance is the ability for a battery to be fully charged or discharged quickly. If 1C is the rate of charge that takes 1 hour to reach full capacity, then high C-rate of 5C is a charging rate that takes 12 minutes to reach full capacity. High C-rate performance of thick electrodes is limited by ion transport [21].

It has been demonstrated that advanced manufacturing techniques can improve ion transport through tailored secondary structures with inbuilt porosity [21,22]. Likewise, these techniques can help prevent binder migration and enhance conductivity networks within the electrode. Such techniques can be further employed to increase energy density of thin electrodes by reducing porosity through improved packing of the components. Solvent-free manufacturing of electrodes is gaining traction in lithium ion battery research. However, dry processing is also susceptible to heterogeneity in the electrode microstructure, through segregation of the primary materials. Hence, local control over the microstructure is also important for dry manufacturing of electrodes. Operation of these advanced manufacturing techniques can be complex, energy intensive, and not very scalable to industrial applications [13,15].

Spherical agglomeration offers one such tool for achieving local control over the electrode microstructure. This technique originated in the coal industry as a separation technique for carbon [23]. More recently the concept has been expanded in the research stage for particle engineering of pharmaceutical products such as paracetamol or salicylic acid [24,25]. Spherical agglomeration is

primarily a process intensification technique that improves handling of primary particles [23]. It has potential for use in pre-formulating multiple components (APIs, excipients) into structured agglomerates. Such agglomerates will improve the flowability of difficult to handle powders and are easier to compress into tablets [26–28]. Agglomerates containing all required components improve the component distribution in a tablet and content uniformity between different tablets. The process is highly scalable and operates at a low energy intensity (room temperature and pressure), making it a suitable alternative to other advanced manufacturing techniques.

Since a battery electrode contains multiple components, spherical agglomeration is a good candidate technique for obtaining structured multicomponent agglomerates. Such agglomerates containing active material, carbon additive, and polymer binder can then be used to achieve local control over the electrode microstructure. Spherical agglomeration offers good control over the properties of formed agglomerates much like other advanced manufacturing techniques such spray drying and fluid bed granulation. However, where spray drying and fluid bed granulation often require high temperature or pressures, spherical agglomeration is less energy intensive - operating at ambient conditions [13,15].

This work demonstrates how spherical agglomeration has been employed as a method for consolidating multicomponent electrode particulate materials into structures agglomerates to achieve local control. A variety of tailored agglomerate structures are generated to demonstrate control over agglomerate properties such as porosity, strength, size, and homogeneity. A novel method of generating active material – carbon black co-agglomerates is presented. We propose that through this co-agglomeration procedure, electrode homogeneity can be improved and electronic conductivity networks can be enhanced by linking intra-agglomerate carbon black (carbon black species within the agglomerate) with inter-agglomerate carbon black (carbon black species between neighboring agglomerates). The relationship between operating parameters and agglomerate properties is investigated through mechanistic understanding of the spherical agglomeration process. The following section outlines the spherical agglomeration technique and adaptation of the underlying procedure to battery materials.

1.1 Spherical Agglomeration

Similar to other granulation techniques, spherical agglomeration utilizes a bridging liquid that binds primary particles together to form agglomerates. The bridging liquid is commonly added directly to precipitating crystals in solution, or is present in one of the solvents involved during crystallization. Alternatively, the bridging liquid can be added to a system of pre-manufactured particles suspended in solution. This method is termed agglomeration-in-suspension, and is employed in this work for the agglomeration of electrode materials.

The agglomeration-in-suspension technique starts with a suspension of primary particles to be agglomerated in a continuous liquid phase. Another phase known as the bridging liquid is then dispersed in the primary particle suspension [25,29,30]. The bridging liquid is chosen such that it is immiscible

with the continuous phase and the primary particles have preferential wettability towards it. Due to continuous stirring inside a stirred tank, injected bridging liquid is broken up into multiple small droplets inside the continuous phase. These then interact with the particles dispersed within the continuous phase through either the distribution mechanism or the immersion mechanism [31].

Figure 1a shows the difference between the immersion and distribution mechanisms. If the bridging liquid droplet size is smaller than the primary particle size, agglomeration can occur via the distribution mechanism. In the distribution mechanism, the bridging liquid droplets thus formed are adsorbed onto the surface of primary particles. During frequent collisions, primary particles become connected to each other through these adsorbed bridging liquid droplets. Agglomeration is expected to stop when there are no free bridging liquid droplets to further connect the primary particles together [31].

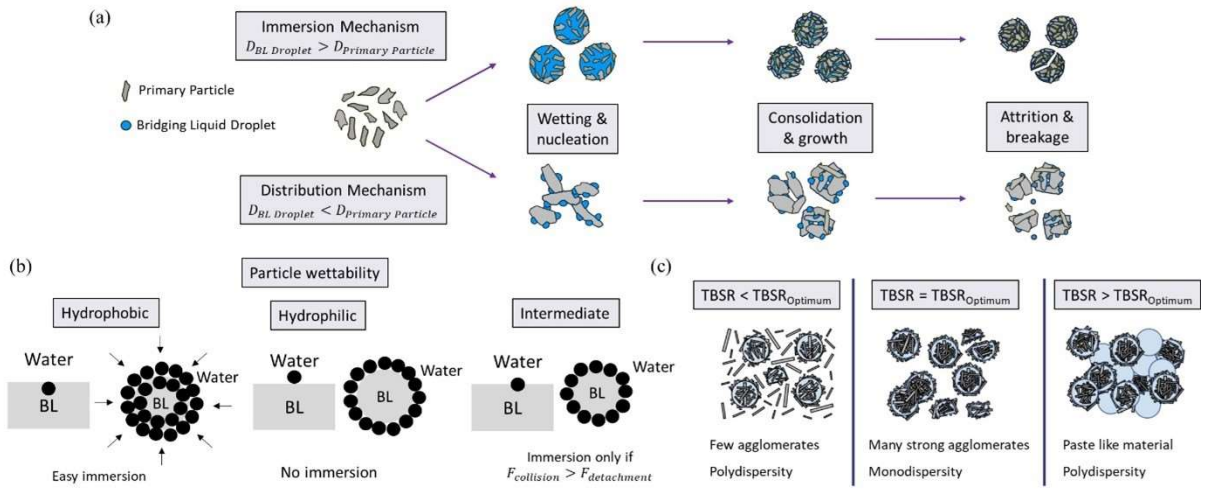

Figure 1: (a) Immersion vs distribution mechanism of spherical agglomerates (Adapted from *[31]*). (b) Particle wettability governs immersion inside the bridging liquid droplet. (c) Effect of true bridging liquid to solids ratio (TBSR) on spherical agglomeration. (Adapted from Tew et al. *[32]*).

Alternatively, if the bridging liquid droplets are larger, particles in the suspension can become immersed into droplets due to frequent collisions. The immersion process is continued until no more particles can be accommodated inside the bridging liquid droplet. When enough primary particles are present, consolidation occurs due to multiple collisions. During consolidation, the bridging liquid will be squeezed out to the agglomerate surface and further growth through layering of primary particles can occur. Equally, as residual bridging liquid remains on the surface of the agglomerates, coalescence can also occur where two or more agglomerates bind together [23]. Eventually, an equilibrium size is achieved for the agglomerates where no layered growth or coalescence between agglomerates occurs, due to a lack of bridging liquid available for interactions. These consolidated agglomerates can then be recovered through filtration and drying. Agglomerate properties such as size and porosity depend strongly on the process parameters [23]. Figure 2a qualitatively shows different stages and mechanisms behind the complete agglomeration-in-suspension process.

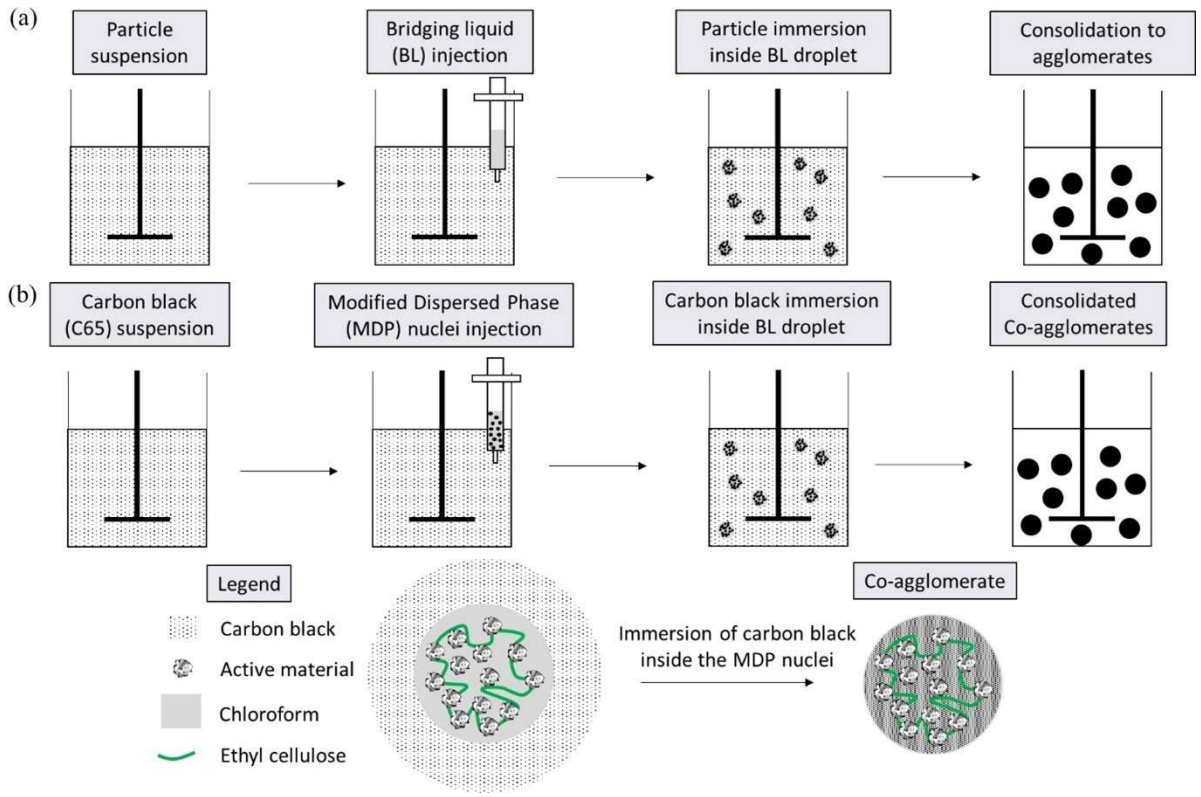

Figure 2: (a) Stages of spherical agglomeration process. (b) Modified dispersed phase method for obtaining AM-CB co-agglomerates.

If the primary particles are partially soluble in the bridging liquid, agglomerates are typically bound together with solid crystal bridges in the dry agglomerate. These solid crystal bridges occur due to evaporative precipitation of the crystals from the bridging liquid. Alternatively, primary particles may be bound together with the help of polymers dissolved in the bridging liquid phase. This polymer solidifies during drying, thus binding the primary particles together.

Agglomerates formed via the immersion mechanism are expected to be proportional in size to the initial bridging liquid droplet size, whereas those generated using the distribution mechanism are expected to generate large agglomerates with no direct relation to the initial bridging liquid droplet size. Arjmandi-Tash et al. [31] have theoretically demonstrated the difference between these two mechanisms and how agglomerate size is correlated to different parameters involved in the mechanism. The work described herein is firmly in the immersion mechanism as the primary particles are substantially smaller than the bridging liquid droplets. The nucleation of spherical agglomerates by immersion mechanism model developed by Arjamandi-Tash et al. [31] is applied in this work to obtain qualitative trends between process parameters and agglomerate properties. Where suitable, these trends are compared with experimental observations.

Particle wettability is a major factor driving the success of the agglomeration process (Figure 1b). Suspended particles need to have preferential wettability towards the bridging liquid to enable particle

immersion and thus agglomeration [23,31]. For example, with water as the continuous phase and organic solvent as the bridging liquid (dispersed phase), hydrophobic particles initially in the continuous phase will immerse inside the bridging liquid droplet upon droplet-particle collision. However, hydrophilic particles will remain in the continuous phase upon droplet-particle collision. It is known that particles exhibiting intermediate wettability prefer to stay on the liquid-liquid interface – a phenomenon enabling formation of Pickering emulsions [33]. For such particles, immersion inside the bridging liquid droplet will occur only if the droplet-particle collision forces ($F_{collision}$) are larger than the detachment forces required to move the particles away from the liquid-liquid interface ($F_{detachmen}$) [34].

While particle wettability and collision forces drive the onset of agglomeration, the True Bridging Liquid to Solids ratio (TBSR) given by Eq. (1) governs the properties of formed agglomerates [23,31].

$$TBSR = \frac{V_{BL}^{available}}{V_{solids}^{continuous\ phase}} = \frac{V_{BL} - V_{BL}^{soluble}}{V_{solids}^{continuous\ phase}} \quad (1)$$

Here, V_{BL} is the volume of the injected bridging liquid. $V_{BL}^{available}$ is the volume of bridging liquid available for agglomeration accounting for solubility of the bridging liquid in the continuous phase, $V_{BL}^{soluble}$ and $V_{solids}^{continuous\ phas}$ is the volume of solid particles suspended in the continuous phase.

For low TBSR, few agglomerates are generated and many unagglomerated primary particles are obtained due to insufficient bridging liquid to agglomerate all the primary particles. For very high TBSR, an over-wetted paste is obtained due to continuous agglomerate coalescence during collisions. Figure 1c schematically shows the effect of TBSR on the obtained agglomerate properties. The TBSR needs to be in the optimum range to achieve monodisperse agglomerates with good consolidation.

Other factors including material properties (e.g. true density of the primary particles, density and viscosity of the bridging liquid relative to the continuous phase, evaporation rate of the bridging liquid) and equipment operating parameters (e.g. impeller speed, impeller clearance, agglomeration time) affect the agglomeration process and properties of the agglomerates formed. Previous studies discuss these dependences in detail [23,31]. pH of the continuous phase can affect the nano-particle suspension hence the agglomeration process [35], but such dependance on the pH is out of scope of the current work.

2. Experimental section

2.1 Materials

A variety of Li-ion battery materials (active materials and carbon black) were used in this work. Material supplier, particle size distribution (PSD), and true density data are tabulated in Table 1. The PSD was measured through wet cell of the Malvern Mastersizer 3000 and Micromeritrics AccuPyc (He pycnometry) was used to measure the true density. Accurate particle size measurements of carbon black nanoparticles were found to be difficult due to the tendency of nanoparticles to aggregate together, therefore an average size range is given from literature [36]. Chloroform (Sigma-Aldrich) was used as the bridging liquid, while ethyl cellulose polymeric binder (Sigma-Aldrich) enhanced stability during the generation of active material (AM) - carbon black (CB) co-agglomerates.

Table 1: Li-ion battery materials used in this work.

Material	**Supplier**	**Particle Size (µm)**			**True Density (g/cm^3)**
		D_{10}	**D_{50}**	**D_{90}**	
Carbon black C65	Imerys	0.03 – 0.05 [36]			1.91 ± 0.0086
$LiFePO_4$ (LFP)	Pi-KEM	0.55	1.46	3.73	3.58 ± 0.0057
NMC 622	Pi-KEM	2.48	4.96	9.17	4.51 ± 0.0021
Synthetic graphite S3	BTR	7.67	16.1	31.1	2.27 ± 0.0027

Here C65 refers to the BET surface area of carbon black nano particles being around 65 m2/g. NMC622 contains 60% Nickel, 20% Manganese, and 20% Cobalt. While S3 refers to the product code from BTR. All particulate materials were stored in the drying cabinet at 60 ºC. Materials were ground in mortar and pestle before being characterized or used in the spherical agglomeration process.

2.2 Carbon black agglomeration

A stirred vessel with four baffles and top lid was used as the agglomeration vessel. A Rushton turbine was selected as the impeller. This turbine creates a double loop radial flow field through the tank. It has been shown that a baffled tank with a Rushton turbine can generate a good flow field without vortices enabling Brownian motion of the suspended primary particles [37]. This uniform flow field is expected to disperse the primary particles and bridging liquid droplets uniformly in the tank. Additionally, the generated flow field should enable frequent collisions between the primary particles and the bridging liquid droplets thus aiding the agglomeration process.

Due to the high hydrophobicity exhibited by the carbon black nanoparticles [38], it is an ideal candidate for spherical agglomeration with water as the continuous phase. Carbon black is difficult to disperse in water [39]; hence some pre-processing is required for sufficient dispersion. Here, the desired amount of carbon black was added in a small vial containing approximately 20 g of DI water. This vial was hand-shaken vigorously and sonicated for 3 min in the sonication bath. Contents of the vial were then poured in another beaker containing 100 g of DI water. The resulting suspension was ultra-sonicated with a high power (500 W) sonication probe for 2 min in pulse mode (on for 5 s then off for 5 s) at 80 % amplitude. After this step, the suspension (120 g) was added to the vessel containing 80 g of DI water. Due to the tendency of the carbon black particles to form aggregates and float on the surface of

the water, impeller clearance was kept high (20 mm) to ensure draw-down and dispersion of the floating particles. Every effort was made to reduce the time gap between ultra-sonication and injection of the bridging liquid under stirring. This ensured minimized re-aggregation of the dispersed carbon black particles in the vessel. The formed carbon black agglomerates were gently poured through a sieve (mesh size: 32 µm or 45 µm) and dried overnight at 60 °C in a drying cabinet. Table 2 gives material quantities and operating conditions used for the generation of carbon black agglomerates. Four different quantities of the bridging liquid (chloroform) were used to investigate the effect of TBSR on carbon black agglomerates. The TBSR values are calculated through Eq. (1) based on volume of injected chloroform ($V_{chloroform}$), volume of chloroform soluble in water ($V_{chloroform}^{Soluble}$) given that the solubility of chloroform in water is 8.09 g/L, and volume of carbon black particles in water ($V_{carbon\ black}^{water}$). Three batches of agglomerates were generated and characterized (size distribution, porosity, tapped density and yield) at each TBSR value.

Other types of conductive additives like carbon black C45, carbon nanotubes, graphene are also used in the battery industry. Depending on the material properties like particle size, surface treatment and topology particle wettability and therefore the agglomeration behavior is expected to be different.

Table 2: Material quantities and operating parameters for generation of C65 agglomerates.

Continuous Phase (CP)	Water	200 mL			
	Carbon black (C65)	0.4 g			
Dispersed Phase (DP)	Chloroform	1.5 mL	2.24 mL	3 mL	5 mL
Operating Parameters	Impeller type	Rushton Turbine			
	Impeller speed	1000 RPM			
	Impeller clearance	20 mm			
	Agglomeration time	10 min			
Derived Parameters	Solids loading	0.2%			
	TBSR	2	5.5	9.2	18.6

2.3 Active material-carbon black co-agglomeration

The agglomeration method in section 2.2 was modified to enable co-agglomeration of active material (AM) and carbon black (CB) C65 particles. The bridging liquid (BL) was modified by dispersing active material particles in it, prior to the injection into the stirred vessel. Some ethyl cellulose (~ 0.6 wt%) was dissolved in the chloroform to act as polymer binder in the generated AM-CB co-agglomerates. Increasing the ethyl cellulose content can strengthen the co-agglomerates, but at the cost of reduced energy density of the final electrode. After injection of this modified dispersed phase (MDP) into the suspension of carbon black particles, small bridging liquid droplets containing active material particles, termed 'MDP nuclei' hereafter, formed. During stirring, the hydrophobic carbon black particles surrounding these MDP nuclei become immersed in the MDP nuclei. Figure 2b schematically shows

the steps involved in this modified dispersed phase method along with the co-agglomeration mechanism. Due to the collisions induced by stirring, consolidation occurs and AM-CB co-agglomerates can be generated.

Table 3 shows the material quantities and operating conditions used for the generation of LFP-C65 co-agglomerates. Ratio of LFP:C65 was kept at 90:10, as this ratio is representative of AM:CB ratio in LFP based cathodes [40]. Operating conditions such as impeller speed, agglomeration time and solids loading were varied to investigate their effect on generated co-agglomerate properties. 'Baseline' values of parameters are indicated in bold. When changing one parameter other parameters were kept at respective baseline values. It should be noted that although the dispersion of LFP particles in the chloroform droplets influence the properties of the disperse phase such as dispersed phase volume fraction (φ_d^{MDP}, Eq. **Error! Reference source not found.**), density (ρ_d^{MDP}, Eq. **Error! Reference source not found.**), viscosity (μ_d^{MDP}, Eq. **Error! Reference source not found.**); the solids loading and TBSR calculations in Table 3 are performed based on the amount of carbon black particles in the continuous phase ($V_{carbon\ black}^{water}$) because the co-agglomeration still occurs through immersion of carbon black particles inside the chloroform. Three batches of co-agglomerates were generated and characterized (size distribution, porosity, tapped density and yield) at each set of operating parameters.

Table 3: Material quantities and operating parameters for generation of LFP-C65 co-agglomerates.

Continuous Phase (CP)	Water	200 ml			
	Carbon black (C65)	0.1 g	**0.2 g**	0.4 g	
Modified Dispersed Phase (MDP)	Chloroform	2.35 mL	2.7 mL	**3 mL**	5 mL
	Ethyl Cellulose	0.6 wt% of chloroform			
	$LiFePO_4$ (LFP)	0.9 g	**1.8 g**	3.6 g	
Operating Parameters	Impeller type	Rushton Turbine			
	Impeller speed	700 RPM	**1000 RPM**	1250 RPM	1500 RPM
	Impeller clearance	20 mm			
	Agglomeration time	**10 min**	20 min	40 min	
Derived Parameters	Solids loading	0.5%	**1.0%**	2.0%	
	TBSR	2.09	2.67	**3.16**	6.47

2.4 Agglomerate Characterization

An optical microscope of 7x magnification was employed for observation of the generated co-/agglomerates. A selection of co-/agglomerates from each batch were broken using a thin spatula to examine the cross-section. The size distribution of the co-/agglomerates was measured through static image analysis. A Canon EOS 2000D (24 MP) camera was used to capture high resolution images (80 px/mm) of co-/agglomerates spread onto a grid. Backlighting was used to eliminate any shadow effects in captured images. For obtaining sharp 2D images of predominantly black agglomerates, wide aperture (f/5.6) was used along with fast shutter speed (1/4000) and high ISO (6400). A total of 48 images were

captured for each batch of co-/agglomerates. This resolution is sufficient to accurately capture size related data for particles of size >150 μm [41], which is the case for most of the co-/agglomerates generated in this work. It should be noted that no sampling protocol was needed as all the co-/agglomerates generated from a specific batch were imaged. The camera setup, agglomerate counting algorithm, and validation of this static image analysis method is shown in section S.1 of the supporting information.

Co-/agglomerate porosity was determined through a combination of He pycnometry and Mercury Intrusion Porosimetry (MIP). For He pycnometry, around 10-20 co-/agglomerates were sampled from the whole batch and placed inside the sample holder. Standard operating protocol was followed to measure the true density. For MIP, around 80% of co-/agglomerates were placed inside the 15 cm^3 powder penetrometer and standard operating protocol was followed for analysis. It should be noted that characterisation sequence of static image analysis, He pycnometry, and finally MIP was followed for each batch of generated co-/agglomerates. After MIP, the co-agglomerates were disposed of as hazardous waste containing mercury.

Porosity (φ) was calculated from the true density (ρ_{True}) and envelope density ($\rho_{Envelope}$) as,

$$\varphi = \left(1 - \frac{\rho_{Envelope}}{\rho_{True}}\right) \times 100 \quad (2)$$

Where the true density (ρ_{True}) is measured from He pycnometry and the envelope density ($\rho_{Envelope}$) is measured from MIP at low pressure (1-2 psi).

The tapped density of generated co-/agglomerates was measured by pouring known weight of the co-/agglomerates into a 5 ml graduated cylinder, such that H/D ≈ 2. The cylinder was tapped 100 times on to a flat benchtop and volume of the tapped sample was measured. The weight of the sample divided by this volume gave the tapped density.

3. Results and Discussion

3.1 Generated structured agglomerates

3.1.1 Carbon Black (CB) agglomerates

After injection of the bridging liquid (chloroform), it is broken down into small droplets under the continuous stirring. Carbon black nano-particles become immersed into these small droplets soon after the injection. High hydrophobicity of the carbon black particles aids the immersion process. As shown in Figure 3, 15 min after chloroform injection, the suspension becomes transparent with the impeller becoming visible.

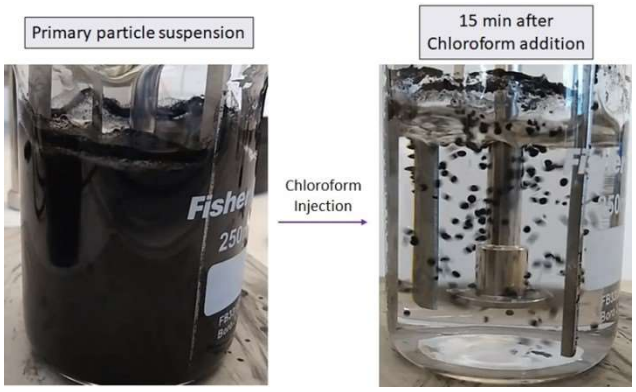

Figure 3: Carbon black suspension becomes transparent after chloroform injection.

As discussed earlier, the amount of the bridging liquid quantified through TBSR value significantly affects the agglomeration process. Agglomeration of carbon black C65 was compared for 4 different TBSR values. It was observed that for TBSR = 18.6 (5 ml chloroform), a paste was formed at the end of the agglomeration process. Agglomerates from the remaining three TBSR values are shown in Figure 4. For TBSR = 2, a significant amount of un-agglomerated material was recovered and very few spherical agglomerates were obtained (Figure 4a). Compared to Figure 1c, it can be said that TBSR = 2 is less than optimum TBSR for the C65 agglomeration. While for TBSR = 5.5 (Figure 4b) and TBSR = 9.2 (Figure 4c), round spherical agglomerates with smooth surface were obtained. This indicates that the optimum TBSR for C65 agglomerates lies in the 5.5-9.2 range.

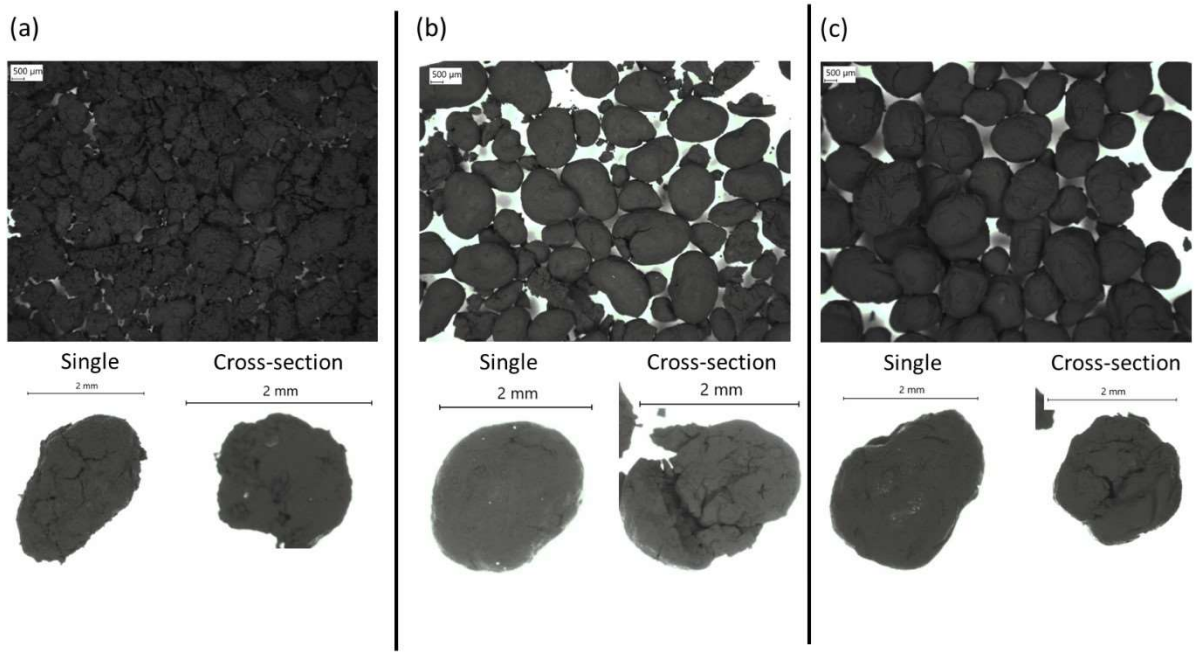

Figure 4: (a) Generated carbon black agglomerates, single agglomerate, and agglomerate cross-section for TBSR = 2, (b) TBSR = 5.5, and (c) TBSR = 9.2.

Static image analysis detected a total of 7380 ± 2697 entities for TBSR = 2 based on the three repeat experiments, compared to 1344 ± 73 entities for TBSR = 5.5 and 680 ± 87 for TBSR = 9.2. The number of entities are expected to decrease with TBSR shifting towards the optimum range as the proportion of un-agglomerated material reduces. As seen from Figure 5a and Figure 5b, a significant size difference is observed between agglomerates from the three TBSR batches. A broad size distribution is observed for the TBSR = 2 batch, while a relatively narrower distribution is observed for TBSR = 5.5 and TBSR = 9.2 batches (Figure 5a). The area weighted median agglomerate size (D_{50}) increased with increasing TBSR values. The TBSR = 5.5 batch shows the least variability between the three repeat experiments (Figure 5b), suggesting that the value of 5.5 is closer to the actual optimum TBSR value compared to 9.2.

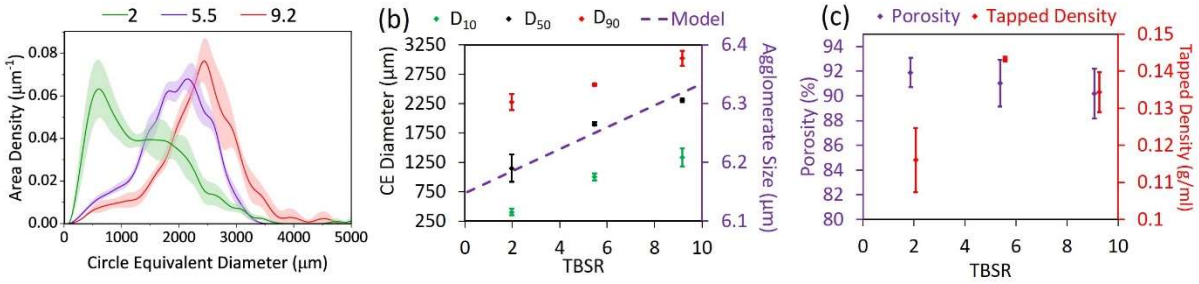

Figure 5: (a) Area weighted differential size distribution, (b) Area weighted D_{10}, D_{50}, D_{90} and theoretical prediction of agglomerate size, (c) Porosity and tapped density for C65 agglomerates generated at three TBSR values (TBSR = 2, TBSR = 5.5, TBSR = 9.2).

Porosity and tapped density measurement results are shown in Figure 5c. Total porosity remains similar with increasing TBSR values. A very high porosity (~90 %) was observed at all TBSR values. Such high porosity of the carbon black agglomerate is speculated to be due to the tendency of carbon black particles to form chains and aggregates that enables interior void formation [39]. It is evident that the collision forces generated during stirring were not sufficient to break the nanoparticle aggregates/chains and pack them densely into the agglomerate. This phenomenon also explains the relatively high value of $TBSR_{Optimum}$ observed for the carbon black agglomerates in comparison to the agglomeration of pharmaceutical powders [23,31]. As shown in Figure 6a, dense packing of particles in the bridging liquid droplet results in larger volume fraction occupied by the particles compared to the loose packing scenario of Figure 6b. Loose packing is expected for nano-particles due to dominant Van der Waals forces resulting in increased tendency to flocculate and form chains. While dense packing is expected in larger particles due to reduced dominance of Van der Waals forces [42]. Assuming that only 10 % of the total agglomerate volume is occupied by C65 particles due to bad packing and remaining 90 % is occupied by the bridging liquid,

$$TBSR_{Optimum} = \frac{V_{BL}^{available}}{V_{particles}} = \frac{0.9V_{total}}{0.1V_{total}} = 9 \quad (3)$$

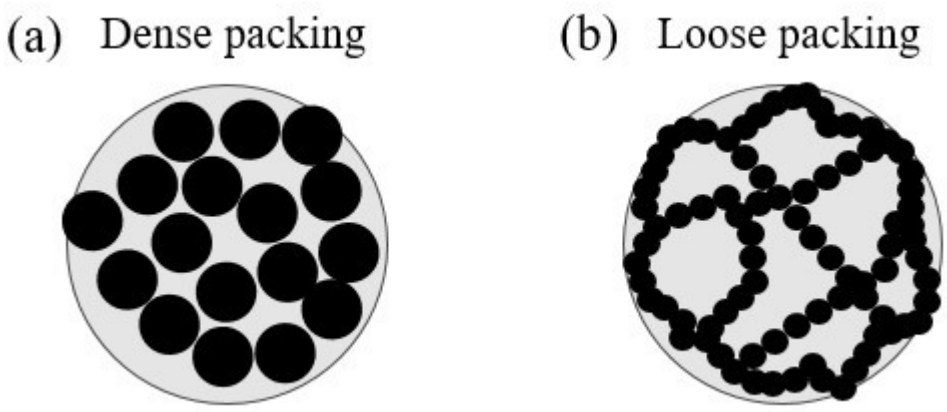

Figure 6: Schematics showing particle packing inside bridging liquid droplet: (a) Dense packing and (b) Loose packing.

An increase in tapped density is observed with increasing the TBSR from 2 to 5.5. This might be due to bad packing caused by relatively non-spherical agglomerates obtained for TBSR = 2 batch. The tapped density for TBSR = 5.5 and TBSR = 9.2 batch is very similar, indicating both values being near the optimum range.

Predictions of the mathematical model for nucleation of spherical agglomerates by the immersion mechanism are also shown in Figure 5b. Derivation of this mathematical model can be found in the work by Arjmandi-Tash et al. [31]. Equations and parameter values used in this work can be found in section S.2 and Table S1 of the supporting information. It can be observed that the model predictions qualitatively agree with experimental observations of increasing agglomerate size with increasing TBSR. As the TBSR is increased, the volume fraction of dispersed phase (φ_d) increases, which results in larger droplet diameter (D_d) as obtained from Eq. (S14). Hence, the agglomerate size given by Eq. (S1) increases with increasing TBSR. The model vastly under-predicts the agglomerate size compared to the experimentally observed agglomerate size. This is expected as the coalescence of agglomerate nuclei is neglected in the model framework. Additional factors such as the sticking of the bridging liquid to the vessel baffles, possible evaporation of the bridging liquid during stirring are not taken into account in the mathematical model resulting in qualitative rather than quantitative predictions.

Although carbon black particles agglomerate successfully in the water (continuous phase) – chloroform (bridging liquid) system, these agglomerates cannot be used directly to control the electrode microstructure. However, C65 agglomerates are useful in terms of improving the flowability and eliminating dust hazards of the fine carbon black powders. Potential applications of these carbon black agglomerates include easier clean handling, elimination of dust hazards, improved flowability and compressibility.

It can be speculated that the size of these agglomerates can be reduced by changing the agglomeration setup. More complex agglomeration setup involving microfluidic junctions for small nuclei generation and agglomeration in a very high-speed homogeniser like stirring system can potentially generate agglomerate with size less than 50 µm. Such small agglomerates can then be directly incorporated into the electrode microstructure.

3.1.2 Active Material (AM) – Carbon Black (CB) co-agglomerates

Based on the modified dispersed phase method discussed in the experimental section, LFP($LiFePO_4$)-C65 co-agglomerates were generated. Similar to the C65 agglomerates, TBSR plays an important role in the LFP-C65 co-agglomeration process. As shown in Table 3, four TBSR values were tested for co-agglomeration of LFP with C65. It should be noted that a certain minimum amount of chloroform is required to accommodate the LFP particles and to enable the pouring transfer of thus formed MDP into the stirred vessel. Therefore, TBSR < 2.09 (chloroform < 2.35 ml) was not possible.

Similar to the carbon black agglomeration, a paste was observed for the TBSR = 6.47 (chloroform = 5 mL) case. Co-agglomerates from the remaining three TBSR values (2.09, 2.67, 3.16) are shown in Figure 7. Both $LiFePO_4$ (grey) and C65 (black) particles can be seen randomly distributed in the obtained co-agglomerates. It is speculated that for the TBSR = 2.09 batch, there is a relatively larger number of un-agglomerated carbon black particles in the continuous phase which coat the surface of the co-agglomerates resulting in relatively darker co-agglomerates compared to the other two TBSR values. With increasing TBSR value, co-agglomerates seem to be more homogeneously mixed as evidenced from the cross-sections.

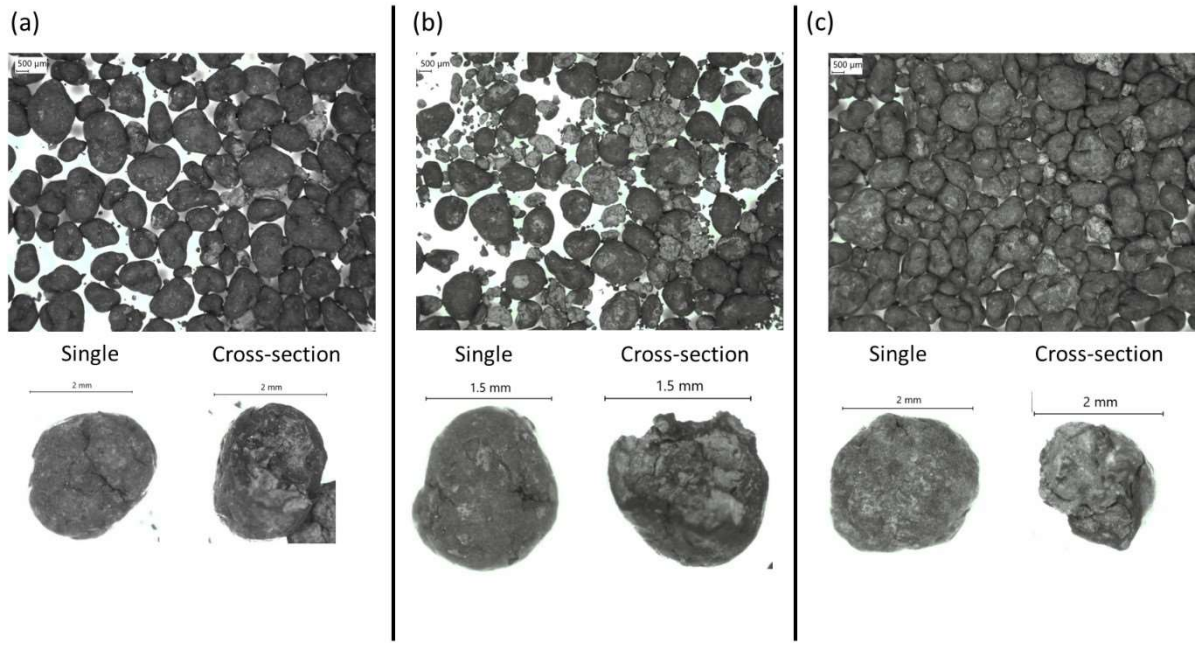

Figure 7: Generated LFP (grey)-C65 (black) co-agglomerates, single co-agglomerate, and co-agglomerate cross-section for (a) TBSR = 2.09, (b) TBSR = 2.67, and (c) TBSR = 3.16.

Figure 8a and Figure 8b shows the size distribution of co-agglomerates obtained from different TBSR values. Since the TBSR values and the amount of injected chloroform are similar to each other, the size distributions of generated co-agglomerates are also similar. The agglomerate counts (2660 ± 376, 2748 ± 387, 2282 ± 58) are also similar between these three batches. For such small range of TBSR variation, co-agglomerate size predicted through the mathematical model (see section S.2) increases slightly due to the increase in droplet diameter of the modified dispersed phase (D_d^{MDP}) given by Eq. (S14) as a result of increasing volume fraction of the modified dispersed phase (φ_d^{MDP}).

Similar porosity and tapped density values are observed for the three TBSR values (Figure 8c). Porosity of LFP-C65 co-agglomerates (~64 %) is much lower than C65 agglomerates (~90 %). This is expected since the LFP particles already occupy about 14.3 % of the initial modified dispersed phase volume and further immersion of C65 particles from the continuous phase should justifiably make the LFP-C65 co-agglomerates denser than the C65 agglomerates.

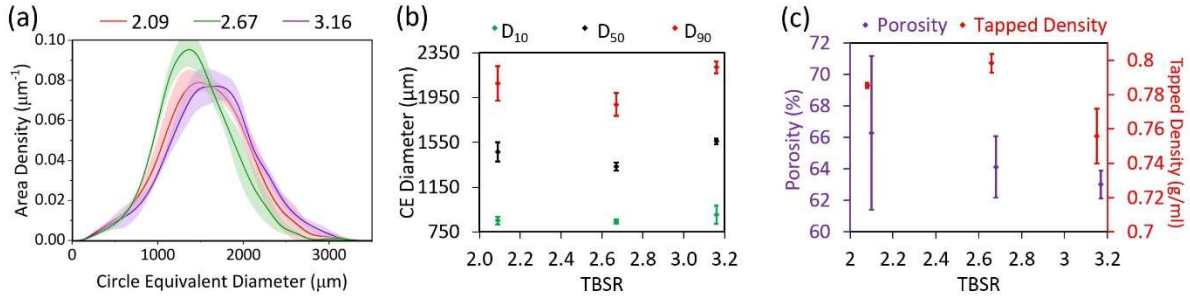

Figure 8: (a) Area weighted differential size distribution, (b) Area weighted D_{10}, D_{50}, D_{90} and theoretical prediction of agglomerate size, (c) Porosity and tapped density for LFP-C65 co-agglomerates generated at TBSR = 2.09, 2.67, 3.16.

Although the distribution and quantification of LFP, C65, and Ethyl Cellulose in each of these co-agglomerates is of interest, accurate quantification would require novel characterization techniques and is out of scope of the current work.

As shown in Figure 9, the modified dispersed phase method can be applied to generate a variety of AM-CB co-agglomerates by varying the active material particles dispersed in the bridging liquid. The distribution of the AM and CB particles inside the co-agglomerate depends on the specific AM-CB particle interactions. A uniform distribution is observed in case of graphite-CB co-agglomerates (Figure 9a). Since graphite is hydrophobic [43], particles remain in the bridging liquid droplet while small C65 particles become immersed in the empty spaces around graphite particles. On the other hand, NMC622 particles exhibit intermediate wettability (Figure 1b), thus they prefer to stay at the liquid-liquid interface rather than inside the droplet. This makes carbon black immersion inside the droplet difficult. Hence resulting co-agglomerates exhibit an approximate core-shell structure where the AM particles are surrounded by the CB particles (Figure 9b).

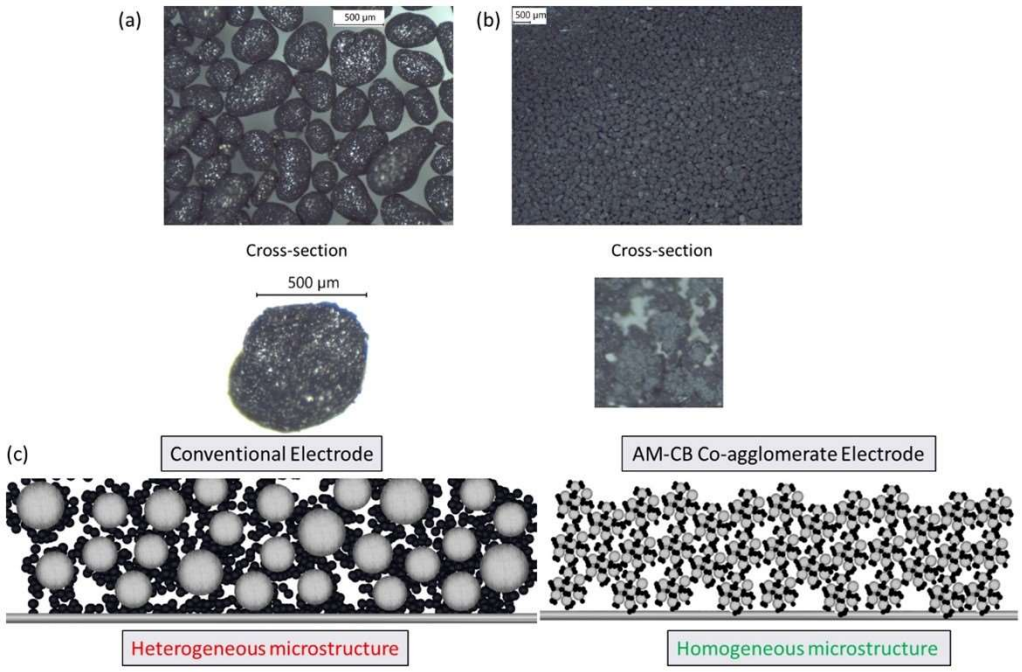

Figure 9: AM-CB co-agglomerates for different AMs. (a) BTR Graphite-C65 co-agglomerate, (b) NMC622-C65 co-agglomerate. (c) Controlling electrode microstructure through AM-CB co agglomerates.

Co-agglomerates obtained using the current agglomeration setup are too big to be incorporated into the electrode microstructure. Similar to the carbon black agglomerates, more complex agglomeration setup involving microfluidic junctions for small nuclei generation and co-agglomeration in a very high-speed homogeniser like stirring system can potentially generate co-agglomerate with size less than 50 µm.

Such AM-CB co-agglomerates if reasonably sized (<50 µm) can form building blocks of the electrode microstructure. Figure 9c schematically demonstrates this concept. If the electrode is made up of such AM-CB co-agglomerates, a more uniform microstructure along the length of the current collector can be obtained. In the next section, the effect of various process parameters on the LFP-C65 co-agglomerate properties are investigated to explore the possibility of generating suitably sized co-agglomerates through tuning of process parameters.

3.2 Controlling co-agglomerate properties

Co-agglomerate properties need to be tuned appropriately to be suitable for incorporation into a battery electrode. These properties often depend on the operating process parameters. To better understand the effect of process parameters on the co-agglomerate size distribution, porosity, and tapped density, different batches of LFP-C65 co-agglomerates were generated by varying operating parameters (agglomeration time, solids loading, impeller speed). When changing one parameter other parameters were kept at respective baseline values reported in Table 3 (in bold). This process-property relationship is elaborated in following subsections. Comparison is made to the agglomerate size predicted by the

theory of spherical agglomeration through immersion mechanism ([31], section S.2) to assess the usefulness of theory in predicting agglomerate size with changing process parameters.

3.2.1 Effect of agglomeration time

Agglomeration time was observed to affect the size distribution of generated LFP-C65 co-agglomerates (Figure 10a and Figure 10b). Most of the agglomeration was observed to occur during the first 10 min after injection of the modified dispersed phase. Co-agglomerates obtained after 10 min agglomeration time were large (D_{50} = 1559 ± 26 µm) and exhibited broad size distribution (Figure 10a). At 20 and 40 min, co-agglomerate size was observed to decrease, mostly likely due to breakage & attrition in the vessel. Although it can be speculated that by increasing the ethyl cellulose content such breakage & attrition can be mitigated, it will come at the cost of reduced energy density in the final electrode (due to increased % of inactive component). Depending on the application, maximum % of ethyl cellulose can be theoretically determined, and corresponding optimum agglomeration duration can be found. It was observed that after 10 min of agglomeration the turbidity of the continuous phase increases. This increase in the turbidity of the continuous phase is thought to be due to two factors. One factor is the migration of LFP particles from the modified dispersed phase nuclei to the continuous phase and the second factor is the breakage of large agglomerates into numerous fragments. The least variability between the three repeat experiments can be observed for 10 min agglomeration time. Static image analysis detected 2282 ± 58 entities at 10 min, while 12185 ± 3021 and 19848 ± 7037 entities were detected at 20 min and 40 min, respectively.

Agglomeration time does not affect porosity and tapped density of the co-agglomerates significantly, as seen in Figure 10c. Due to large variation observed in the porosity and tapped density of the three samples measured, firm conclusions cannot be drawn about the variation of porosity and tapped density with agglomeration time. All these results indicate that 10 min agglomeration time is preferable for obtaining LFP-C65 co-agglomerates with minimal loss of LFP particles from the modified dispersed phase nuclei and minimal attrition.

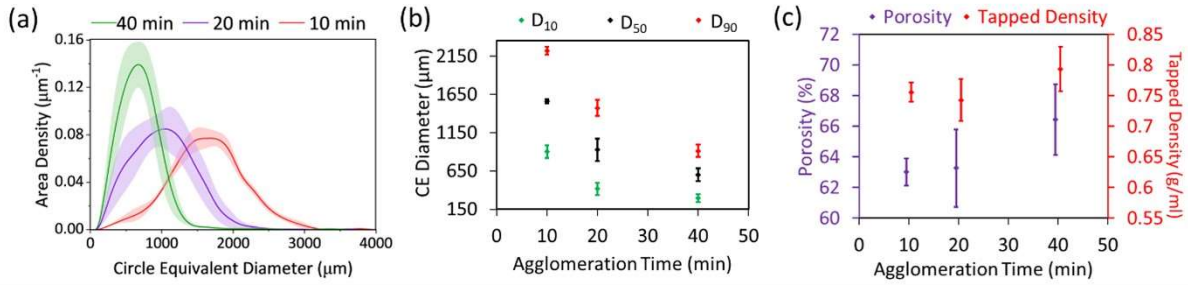

Figure 10: Effect of agglomeration time on (a) Area weighted differential size distribution, (b) Area weighted D_{10}, D_{50}, D_{90}, and theoretical prediction of agglomerate size, (c) Porosity and tapped density of LFP-C65 co-agglomerates generated with 10 min, 20 min, 40 min agglomeration times.

3.2.2 Effect of solids loading

For a fixed TBSR = 3.16, three values of solids loadings were investigated (0.5 %, 1.0 %, 2.0 %). As observed from Figure 11a, more variability was observed between the three repeat experiments at 0.5 % solids loading compared to the other batches. This is expected due to larger relative loss of material during experimentation at 0.5 % solids loading compared to other two batches. This variability between the three batches can be reduced by scaling-up the vessel, but this is out of scope of the current work. At a glance, it looks like the agglomerate size increases from 0.5 % to 1.0 % solids loading but remains similar from 1.0 % to 2.0 % solids loading. However, due to the large variability of 0.5 % solids loading, firm conclusions cannot be drawn about the trend of co-agglomerate size with solids loading (Figure 11b).

Slightly decreasing porosity is observed with increasing solids loading from 0.5 % to 1.0 % (Figure 11c). This is expected as with increasing solids loading (ϕ_{Pb}) the collision rate increases according to Eq. (S10), resulting in more consolidated dense co-agglomerates. The tapped density is therefore expected to increase with solids loading due to denser similarly sized co-agglomerates.

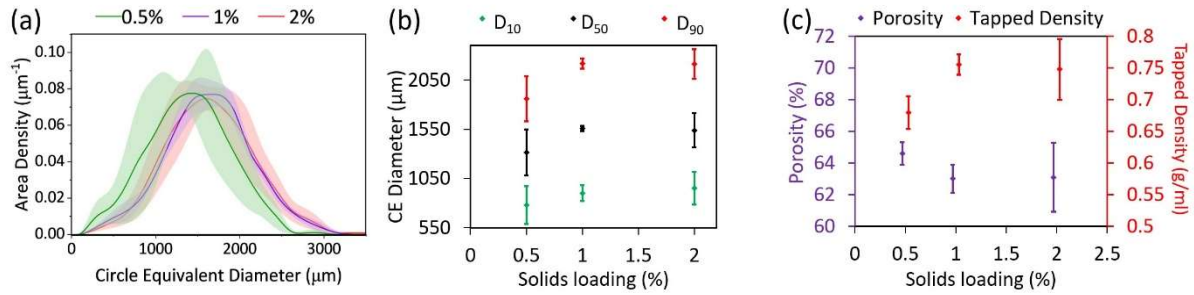

Figure 11: Effect of solids loading on (a) Area weighted differential size distribution, (b) Area weighted D_{10}, D_{50}, D_{90} and theoretical prediction of agglomerate size, (c) Porosity and tapped density of LFP-C65 co-agglomerates generated with 0.5 %, 1.0 %, 2.0 % solids loading.

3.2.3 Effect of impeller speed

Impeller speed significantly affects the size distribution of generated co-agglomerates (Figure 12a and Figure 12b). With increasing impeller speed agglomerate size decreases, most like due to a reduction in the size distribution of the modified dispersed phase nuclei and an increased collision rate causing more breakage of large agglomerates. As shown in Table 3, four impeller speed values (700 RPM, 1000 RPM, 1250 RPM, 1500 RPM) were investigated. It was observed that co-agglomeration was unsuccessful when using an impeller speed of 700 RPM, due to inadequate dispersion of C65 particles and chloroform droplets caused by the poor flow field. At 700 RPM, dense chloroform droplets remain near the beaker base resulting in a paste and no agglomerates. At very high impeller speeds (1500 RPM), air bubble entrapment was observed in the vessel. Air bubble entrapment causes faster evaporation of the injected chloroform, avoidance of coalescence due to large turbulence intensity, and increased breakage due to increased collision rate. All of these factors cause a significant decrease in the co-agglomerate size. Due to the same factors, very high variability was observed at 1500 RPM. Hence, for

reproducible co-agglomeration, air bubble entrapment should be avoided. It should be noted that the least amount of variability between the three repeat experiments was observed at 1250 RPM. Absence of air bubble entrapment along with high collision rate is speculated to be the reason behind this high reproducibility.

No significant difference was observed in the porosity values at different impeller speeds (Figure 12c). The tapped density is highest for 1250 RPM batch which is expected due to denser packing achieved by the smooth spherical agglomerates with a narrow size distribution.

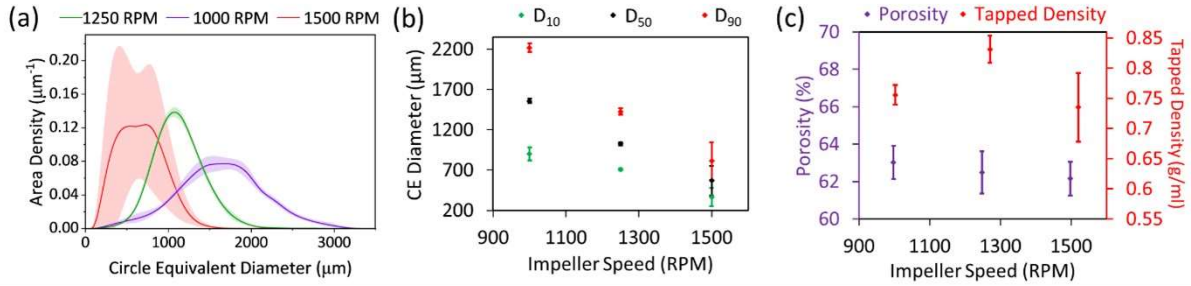

Figure 12: Effect of impeller speed on (a) Area weighted differential size distribution, (b) Area weighted D_{10}, D_{50}, D_{90} and theoretical prediction of agglomerate size, (c) Porosity and tapped density of LFP-C65 co-agglomerates generated at 1000 RPM, 1250 RPM, 1500 RPM.

Based on this investigation, good co-agglomerates were obtained at 10 min of agglomeration time, 1% solids loading, and 1250 RPM of impeller speed. Thorough investigation needs to be done for a different material system to find the respective optimum operating conditions.

4. Conclusions

The technique of spherical agglomeration was applied to Li-ion battery materials. Single component carbon black (C65) agglomerates as well as multi-component active material-carbon black (AM-CB) co-agglomerates were generated. Carbon black agglomerates exhibited very high porosity (~90 %) due to the tendency of nanoparticles to form chains and aggregates enabling interior void formation. LFP($LiFePO_4$)-C65 co-agglomerates exhibited less porosity (~64 %) due to the use of a modified dispersed phase as the bridging liquid for spherical agglomeration.

The effect of different process parameters (agglomeration time, solids loading, impeller speed) on LFP-C65 co-agglomerate properties was investigated. It was observed that 10 min agglomeration time is preferential to minimize loss of LFP particles due to migration from the modified dispersed phase to the continuous phase. Slightly dense co-agglomerates were obtained with increasing solids loading at a fixed TBSR value. This observation conforms with the theoretical equation relating solids loading to the collision rate. Impeller speed was a dominating parameter. Too low impeller speed (700 RPM) results in a poor flow field for which no agglomeration was observed. Too high impeller speed (1500 RPM) can result in air bubble entrapment, causing large variability between repeat experiments. There

exists an optimum range for parameters like the TBSR, agglomeration time, and impeller speed where high yield (> 80%) and narrow size distribution of LFP-C65 co-agglomerates can be obtained.

Although the agglomerate size predicted through the mathematical model for nucleation of spherical agglomerates by the immersion mechanism was two orders of magnitude smaller than experimental value, this model is useful in qualitatively predicting the dependence of agglomerate size on process parameters. The model can be further improved by taking into account the effect of nuclei coalescence, breakage & attrition.

It should be noted that even though the large size of co-/agglomerates generated in this work renders them currently unsuitable for electrode generation, the understanding generated in this work demonstrates the potential to generate smaller agglomerates in the future. The co-/agglomerate in this work may also prove useful in other applications, as they have improved flowability and reduce dust hazards for fine carbon black powders. AM-CB co-agglomerates may be used in the future to reducing the number of steps involved in the process of obtaining homogeneously mixed slurry for electrode coating.

5. Acknowledgements

The authors would like to thank The Faraday Institution for the financial support towards the 'Nextrode' project (Grant Number: FIRG015) and the Summer Undergraduate Research Fellowship (SURF) through the University of Sheffield, Chemical and Biological Engineering Department.

References

[1] K.A. Murashko, A.V. Mityakov, V.Y. Mityakov, S.Z. Sapozhnikov, J. Jokiniemi, J. Pyrhönen, Determination of the entropy change profile of a cylindrical lithium-ion battery by heat flux measurements, Journal of Power Sources 330 (2016) 61–69. https://doi.org/10.1016/j.jpowsour.2016.08.130.

[2] L. Chen, W. Lin, J. Li, B. Tian, H. Pan, Prediction of lithium-ion battery capacity with metabolic grey model, Energy 106 (2016) 662–672. https://doi.org/10.1016/j.energy.2016.03.096.

[3] K. Pardikar, J. Entwistle, R. Ge, D. Cumming, R. Smith, Status and outlook for lithium-ion battery cathode material synthesis and the application of mechanistic modeling, Journal of Physics: Energy 5 (2023) 022002. https://doi.org/10.1088/2515-7655/acc139.

[4] J. Entwistle, R. Ge, K. Pardikar, R. Smith, D. Cumming, Carbon binder domain networks and electrical conductivity in lithium-ion battery electrodes: A critical review, Renewable and Sustainable Energy Reviews 166 (2022) 112624. https://doi.org/10.1016/j.rser.2022.112624.

[5] M. Nikpour, N. Barrett, Z. Hillman, A.I. Thompson, B.A. Mazzeo, D.R. Wheeler, A Model for Investigating Sources of Li-Ion Battery Electrode Heterogeneity: Part I. Electrode Drying and Calendering Processes, Journal of The Electrochemical Society 168 (2021) 060547. https://doi.org/10.1149/1945-7111/ac0bf1.

[6] M. Duquesnoy, I. Boyano, L. Ganborena, P. Cereijo, E. Ayerbe, A.A. Franco, Machine learning-based assessment of the impact of the manufacturing process on battery electrode heterogeneity, Energy and AI 5 (2021) 100090. https://doi.org/10.1016/j.egyai.2021.100090.

[7] M.M. Forouzan, B.A. Mazzeo, D.R. Wheeler, Modeling the Effects of Electrode Microstructural Heterogeneities on Li-Ion Battery Performance and Lifetime, Journal of The Electrochemical Society 165 (2018) A2127–A2144. https://doi.org/10.1149/2.1281809jes.

[8] T. Lombardo, A.C. Ngandjong, A. Belhcen, A.A. Franco, Carbon-Binder Migration: A Three-Dimensional Drying Model for Lithium-ion Battery Electrodes, Energy Storage Materials 43 (2021) 337–347. https://doi.org/10.1016/j.ensm.2021.09.015.

[9] S. Jaiser, M. Müller, M. Baunach, W. Bauer, P. Scharfer, W. Schabel, Investigation of film solidification and binder migration during drying of Li-Ion battery anodes, Journal of Power Sources 318 (2016) 210–219. https://doi.org/10.1016/j.jpowsour.2016.04.018.

[10] M. Müller, L. Pfaffmann, S. Jaiser, M. Baunach, V. Trouillet, F. Scheiba, P. Scharfer, W. Schabel, W. Bauer, Investigation of binder distribution in graphite anodes for lithium-ion batteries, Journal of Power Sources 340 (2017) 1–5. https://doi.org/10.1016/j.jpowsour.2016.11.051.

[11] M. Nikpour, B.A. Mazzeo, D.R. Wheeler, A Model for Investigating Sources of Li-Ion Battery Electrode Heterogeneity: Part II. Active Material Size, Shape, Orientation, and Stiffness, Journal of The Electrochemical Society 168 (2021) 120518. https://doi.org/10.1149/1945-7111/ac3c1f.

[12] B. Vertruyen, N. Eshraghi, C. Piffet, J. Bodart, A. Mahmoud, F. Boschini, Spray-Drying of Electrode Materials for Lithium- and Sodium-Ion Batteries, Materials 11 (2018) 1076. https://doi.org/10.3390/ma11071076.

[13] H. Li, L. Sun, Y. Zhao, T. Tan, Y. Zhang, Blackberry-like hollow graphene spheres synthesized by spray drying for high-performance lithium-sulfur batteries, Electrochimica Acta 295 (2019) 822–828. https://doi.org/10.1016/j.electacta.2018.11.012.

[14] J.-H. Park, S.-W. Kang, T.-S. Kwon, H.S. Park, Spray-drying assisted synthesis of a Li4Ti5O12/C composite for high rate performance lithium ion batteries, Ceramics International 44 (2018) 2683–2690. https://doi.org/10.1016/j.ceramint.2017.10.217.

[15] C. Chen, R. Agrawal, C. Wang, Electrostatic spray deposition of Li 4 Ti 5 O 12 based anode with enhanced rate capability and energy density for lithium-ion batteries, in: N.K. Dhar, A.K. Dutta (Eds.), K, Baltimore, Maryland, United States p. 986507, 2016: p. 986507. https://doi.org/10.1117/12.2228905.

[16] X. Li, C. Wang, Engineering nanostructured anodes via electrostatic spray deposition for high performance lithium ion battery application, J. Mater. Chem. A 1 (2013) 165–182. https://doi.org/10.1039/C2TA00437B.

[17] S.C. Lee, J. Jeong, H.G. Park, B.-C. Min, S. Chan Jun, K.Y. Chung, Binder-assisted electrostatic spray deposition of LiCoO2 and graphite films on coplanar interdigitated electrodes for flexible/wearable lithium-ion batteries, Journal of Power Sources 472 (2020) 228573. https://doi.org/10.1016/j.jpowsour.2020.228573.

[18] Z.D. Gordon, T. Yang, G.B. Gomes Morgado, C.K. Chan, Preparation of Nano- and Microstructured Garnet Li 7 La 3 Zr 2 O 12 Solid Electrolytes for Li-Ion Batteries via Cellulose

Templating, ACS Sustainable Chemistry & Engineering 4 (2016) 6391–6398. https://doi.org/10.1021/acssuschemeng.6b01032.

[19] I. Kokal, E.J. van den Ham, A.C.A. Delsing, P.H.L. Notten, H.T. Hintzen, Preparation and characterization of three dimensionally ordered macroporous Li5La3Ta2O12 by colloidal crystal templating for all-solid-state lithium-ion batteries, Ceramics International 41 (2015) 737–741. https://doi.org/10.1016/j.ceramint.2014.08.132.

[20] C.M. Doherty, R.A. Caruso, B.M. Smarsly, C.J. Drummond, Colloidal Crystal Templating to Produce Hierarchically Porous LiFePO 4 Electrode Materials for High Power Lithium Ion Batteries, Chemistry of Materials 21 (2009) 2895–2903. https://doi.org/10.1021/cm900698p.

[21] H. Gao, Q. Wu, Y. Hu, J.P. Zheng, K. Amine, Z. Chen, Revealing the Rate-Limiting Li-Ion Diffusion Pathway in Ultrathick Electrodes for Li-Ion Batteries, Journal of Physical Chemistry Letters 9 (2018) 5100–5104. https://doi.org/10.1021/acs.jpclett.8b02229.

[22] W. Deng, W. Shi, Q. Liu, J. Jiang, X. Li, X. Feng, Constructing Gradient Porous Structure in Thick Li 4 Ti 5 O 12 Electrode for High-Energy and Stable Lithium-Ion Batteries, ACS Sustainable Chemistry & Engineering 8 (2020) 17062–17068. https://doi.org/10.1021/acssuschemeng.0c04716.

[23] K. Pitt, R. Peña, J.D. Tew, K. Pal, R. Smith, Z.K. Nagy, J.D. Litster, Particle design via spherical agglomeration: A critical review of controlling parameters, rate processes and modelling, Powder Technology 326 (2018) 327–343. https://doi.org/10.1016/j.powtec.2017.11.052.

[24] A.P. Pawar, A.R. Paradkar, S.S. Kadam, K.R. Mahadik, Crystallo-co-agglomeration: A novel technique to obtain ibuprofen-paracetamol agglomerates, AAPS PharmSciTech 5 (2004) 57–64. https://doi.org/10.1208/pt050344.

[25] C. Subero-Couroyer, D. Mangin, A. Rivoire, A.F. Blandin, J.P. Klein, Agglomeration in suspension of salicylic acid fine particles: Analysis of the wetting period and effect of the binder injection mode on the final agglomerate size, Powder Technology 161 (2006) 98–109. https://doi.org/10.1016/j.powtec.2005.08.014.

[26] H. Chen, C. Wang, H. Kang, B. Zhi, C.L. Haynes, A. Aburub, C.C. Sun, Microstructures and pharmaceutical properties of ferulic acid agglomerates prepared by different spherical crystallization methods, International Journal of Pharmaceutics 574 (2020) 118914. https://doi.org/10.1016/j.ijpharm.2019.118914.

[27] N.R. Jadhav, A.P. Pawar, A.R. Paradkar, Preparation and evaluation of talc agglomerates obtained by wet spherical agglomeration as a substrate for coating, Pharmaceutical Development and Technology 16 (2011) 152–161. https://doi.org/10.3109/10837450903544567.

[28] H. Zhang, Y. Chen, J. Wang, J. Gong, Investigation on the Spherical Crystallization Process of Cefotaxime Sodium, Industrial & Engineering Chemistry Research 49 (2010) 1402–1411. https://doi.org/10.1021/ie901001c.

[29] J. Thati, Å.C. Rasmuson, Particle engineering of benzoic acid by spherical agglomeration, European Journal of Pharmaceutical Sciences 45 (2012) 657–667. https://doi.org/10.1016/j.ejps.2012.01.006.

[30] R. Peña, J.A. Oliva, C.L. Burcham, D.J. Jarmer, Z.K. Nagy, Process Intensification through Continuous Spherical Crystallization Using an Oscillatory Flow Baffled Crystallizer, Crystal Growth & Design 17 (2017) 4776–4784. https://doi.org/10.1021/acs.cgd.7b00731.

[31] O. Arjmandi-Tash, J.D. Tew, K. Pitt, R. Smith, J.D. Litster, A new mathematical model for nucleation of spherical agglomerates by the immersion mechanism, Chemical Engineering Science: X 4 (2019) 100048. https://doi.org/10.1016/j.cesx.2019.100048.

[32] J.D. Tew, K. Pitt, R. Smith, J.D. Litster, True bridging liquid-solid ratio (TBSR): Redefining a critical process parameter in spherical agglomeration, Powder Technology 430 (2023) 119010. https://doi.org/10.1016/j.powtec.2023.119010.

[33] B.P. Binks, S.O. Lumsdon, Influence of Particle Wettability on the Type and Stability of Surfactant-Free Emulsions, Langmuir 16 (2000) 8622–8631. https://doi.org/10.1021/la000189s.

[34] R. Ettelaie, S. V. Lishchuk, Detachment force of particles from fluid droplets, Soft Matter 11 (2015) 4251–4265. https://doi.org/10.1039/C5SM00540J.

[35] L. Al-Gebory, M.P. Mengüç, The effect of pH on particle agglomeration and optical properties of nanoparticle suspensions, Journal of Quantitative Spectroscopy and Radiative Transfer 219 (2018) 46–60. https://doi.org/10.1016/j.jqsrt.2018.07.020.

[36] D. Grießl, K. Huber, R. Scherbauer, A. Kwade, Dispersion kinetics of carbon black for the application in lithium-ion batteries, Advanced Powder Technology 32 (2021) 2280–2288. https://doi.org/10.1016/j.apt.2021.05.003.

[37] Q. Zhu, H. Xiao, A. Chen, S. Geng, Q. Huang, CFD study on double- to single-loop flow pattern transition and its influence on macro mixing efficiency in fully baffled tank stirred by a Rushton turbine, Chinese Journal of Chemical Engineering 27 (2019) 993–1000. https://doi.org/10.1016/j.cjche.2018.10.002.

[38] D. Lizonova, U. Trivanovic, P. Demokritou, G.A. Kelesidis, Dispersion and Dosimetric Challenges of Hydrophobic Carbon-Based Nanoparticles in In Vitro Cellular Studies, Nanomaterials 14 (2024) 589. https://doi.org/10.3390/nano14070589.

[39] H. Ridaoui, A. Jada, L. Vidal, J.-B. Donnet, Effect of cationic surfactant and block copolymer on carbon black particle surface charge and size, Colloids and Surfaces A: Physicochemical and Engineering Aspects 278 (2006) 149–159. https://doi.org/10.1016/j.colsurfa.2005.12.013.

[40] A. Gören, C.M. Costa, M.M. Silva, S. Lanceros-Méndez, State of the art and open questions on cathode preparation based on carbon coated lithium iron phosphate, Composites Part B: Engineering 83 (2015) 333–345. https://doi.org/10.1016/j.compositesb.2015.08.064.

[41] M. Đuriš, Z. Arsenijević, D. Jaćimovski, T. Kaluđerović Radoičić, Optimal pixel resolution for sand particles size and shape analysis, Powder Technology 302 (2016) 177–186. https://doi.org/10.1016/j.powtec.2016.08.045.

[42] V.A. Parsegian, Van der Waals Forces: A Handbook for Biologists, Chemists, Engineers, and Physicists, 1st ed., Cambridge University Press, 2005. https://doi.org/10.1017/CBO9780511614606.

[43] A. Kozbial, F. Zhou, Z. Li, H. Liu, L. Li, Are Graphitic Surfaces Hydrophobic?, Acc. Chem. Res. 49 (2016) 2765–2773. https://doi.org/10.1021/acs.accounts.6b00447.

[44] T. Wagner, ParticleSizer ij-particlesizer: ParticleSizer 1.0.1., (2016).

[45] P.M. Orlewski, B. Ahn, M. Mazzotti, Tuning the Particle Sizes in Spherical Agglomeration, Crystal Growth & Design 18 (2018) 6257–6265. https://doi.org/10.1021/acs.cgd.8b01134.

[46] B. Kysela, J. Konfrst, Z. Chara, R. Sulc, D. Jasikova, Evaluation of the turbulent kinetic dissipation rate in an agitated vessel, EPJ Web of Conferences 143 (2017) 02062. https://doi.org/10.1051/epjconf/201714302062.

[47] R. V. Calabrese, C.Y. Wang, N.P. Bryner, Drop breakup in turbulent stirred-tank contactors. Part III: Correlations for mean size and drop size distribution, AIChE Journal 32 (1986) 677–681. https://doi.org/10.1002/aic.690320418.

[48] K.K. Singh, S.M. Mahajani, K.T. Shenoy, S.K. Ghosh, Representative drop sizes and drop size distributions in A/O dispersions in continuous flow stirred tank, Hydrometallurgy 90 (2008) 121–136. https://doi.org/10.1016/j.hydromet.2007.10.003.

[49] A.W. Pacek, S. Chamsart, A.W. Nienow, A. Bakker, The influence of impeller type on mean drop size and drop size distribution in an agitated vessel, Chemical Engineering Science 54 (1999) 4211–4222. https://doi.org/10.1016/S0009-2509(99)00156-6.

[50] G.K. Batchelor, The effect of Brownian motion on the bulk stress in a suspension of spherical particles, Journal of Fluid Mechanics 83 (1977) 97–117. https://doi.org/10.1017/S0022112077001062.

Supporting Information

S.1 Static image analysis setup

The camera setup for measuring co-/agglomerate size through static image analysis is shown in Figure S1. All co-/agglomerates generated from a batch were measured using this setup to avoid any sampling protocol related errors.

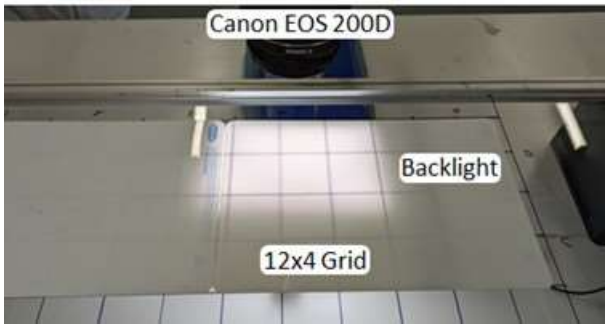

Figure S1: Image acquisition setup for capturing images of generated agglomerates.

Captured images were analysed through the 'ParticleSizer' plugin of open source software ImageJ. This plugin applies multiple image processing steps and watershed segmentation to extract particle shape and size related data [44]. Some steps (Denoising, Homogenization with median filter, Shape smoothing) of the original plugin were disabled as they were unnecessary for the good quality images obtained with current setup. The thresholding method was changed from 'Phansalkar' to 'OTSU'. Other steps (subtracting background, irregular watershed segmentation) were retained as shown in Figure S2. All co-/agglomerates contained in a batch were spread onto the backlit white background such that most co-/agglomerates are separated from each other. This sample preparation was performed to aid the object segmentation. Entities with minimum ferret diameter below $10\ \text{px} \approx 125\ \mu\text{m}$ were ignored during this image analysis.

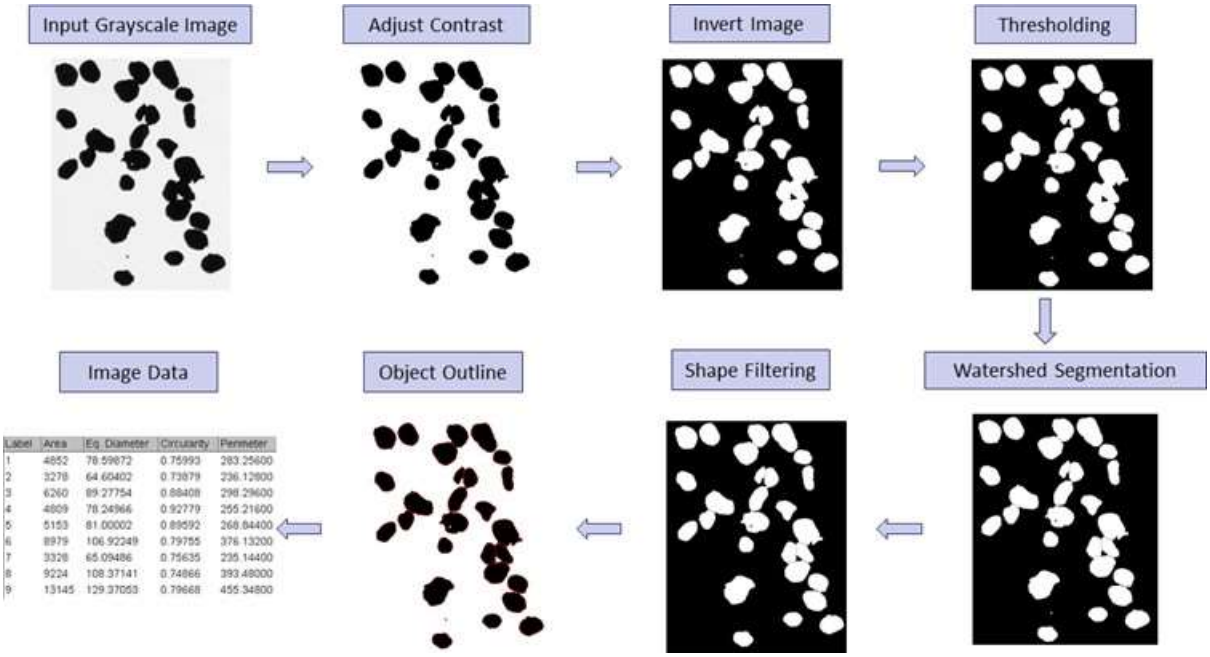

Figure S2: Steps of ImageJ plugin 'ParticleSizer' for the image analysis based agglomerate size measurement *[44]*.

This static image analysis algorithm is validated against spherical particles of known size distribution.

1.5 mm black cellulose acetate Spheres

These precision spheres were obtained from Cospheric. The black spheres accurately resemble the black agglomerates generated in this work. Supplier specifications stated 100 particles with diameters 1500 ± 50 µm. These spheres along with corresponding area weighted PSD are shown in Figure S3.

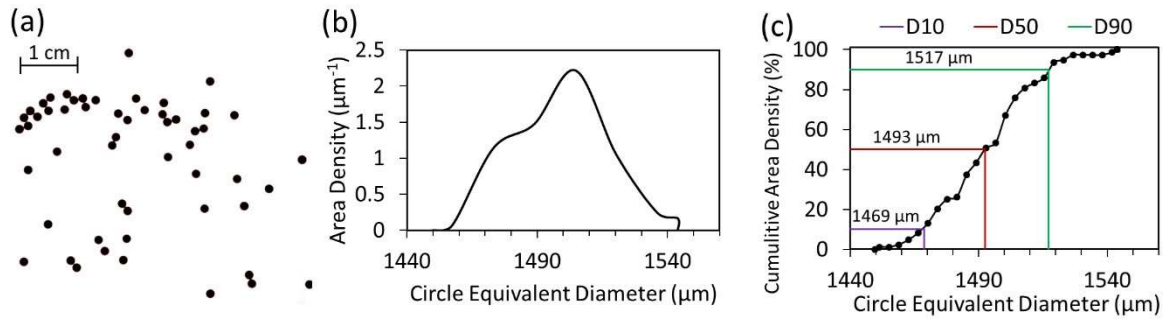

Figure S3: (a) Black cellulose acetate spheres, (b) Area density distribution of circle equivalent diameter obtained from static image analysis, (c) Cumulative area distribution of CE diameter showing D_{10}, D_{50}, D_{90} values.

As seen from Figure S3b, these particles have circle equivalent diameter in the range of 1469 - 1517 µm range. With D50 around 1493 µm. These results indicate that the current setup and image analysis algorithm works well for 1.5 mm diameter particles.

1-1.2 mm Yttrium beads

These yttrium beads are used for ball milling. Supplier specifications indicate that these beads are in the range of 1 to 1.2 mm in diameter. Figure S4 shows an image of these beads and corresponding size distribution.

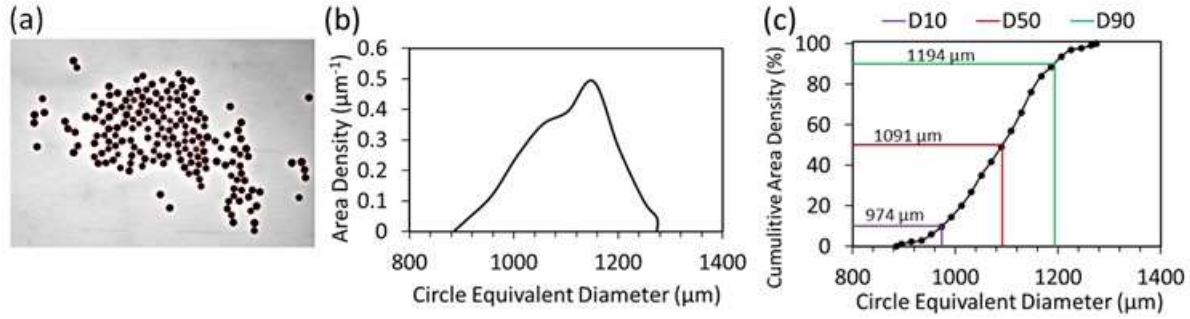

Figure S4: (a) White yttrium beads on black background, (b) Area density distribution of circle equivalent diameter obtained from static image analysis, (c) Cumulative area distribution of CE diameter showing D_{10}, D_{50}, D_{90} values.

As seen from Figure S4b, majority of the yttrium particles have equivalent diameter in the 974-1194 µm range. While D50 is 1091 µm. These results indicate that the current setup and image analysis algorithm works well for 1-1.2 mm diameter particles.

500-600 µm violet polyethylene particles

These microspheres were obtained from Cospheric. Although violet colored they represent opaque agglomerates generated in this work. Supplier specifications stated particles with diameters in the range of 500-600 µm. These spheres along with corresponding area weighted PSD and comparison to PSD measurements made through the Malvern Mastersizer are shown in Figure S5.

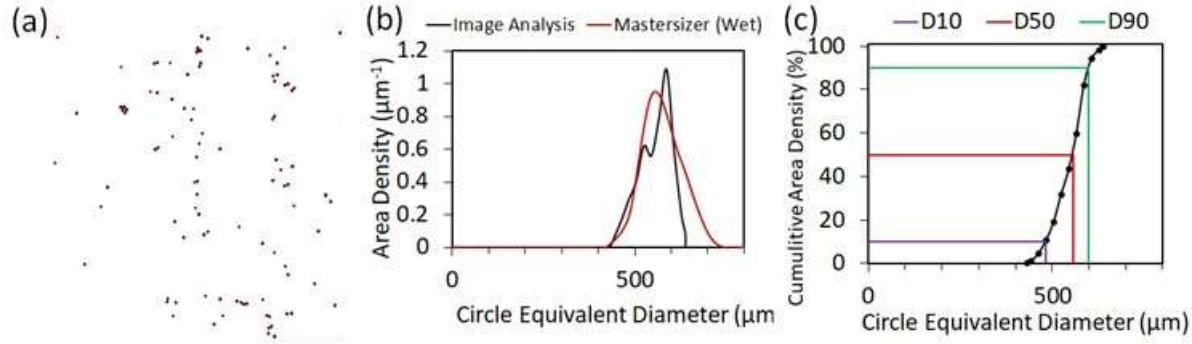

Figure S5: (a) Violet polyethylene spheres on black background, (b) Area density distribution of circle equivalent diameter obtained from static image analysis, (c) Cumulative area distribution of CE diameter showing D_{10}, D_{50}, D_{90} values.

155-190 µm black tungsten carbide particles

These microspheres were obtained from Cospheric. The black spheres accurately resemble the black agglomerates generated in this work. Supplier specifications stated particles with diameters in the range

of 155-190 µm. These spheres along with corresponding area weighted PSD and comparison to PSD measurements made through the Malvern Mastersizer are shown in Figure S6.

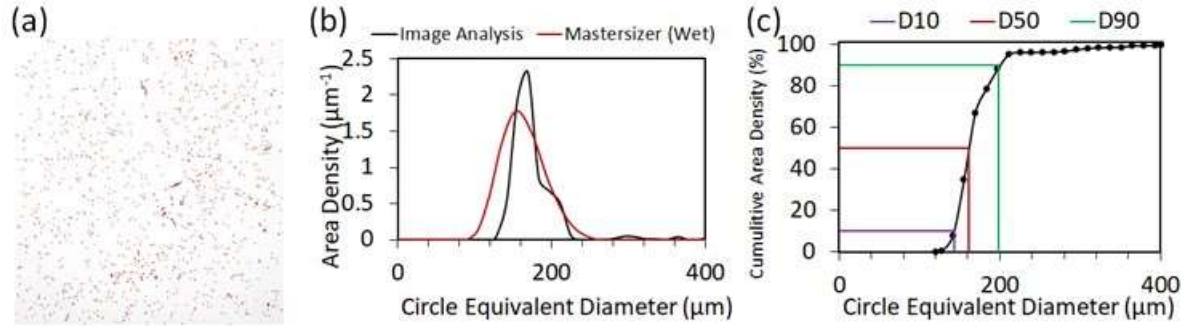

Figure S6: (a) Black tungsten carbide spherical particles, (b) Area density distribution of circle equivalent diameter obtained from static image analysis, (c) Cumulative area distribution of CE diameter showing D_{10}, D_{50}, D_{90} values.

As seen from Figure S6b, majority of the black tungsten carbide particles have equivalent diameter in the 143-199 µm range. While D50 is 162 µm. These results indicate that the current setup and image analysis algorithm works well for 155-190 µm diameter particles. For further validation, size distribution of these particles was also obtained through wet cell mastersizer measurements. Comparison showed results similar to that of image analysis.

Although current image acquisition setup and analysis algorithm was observed to be less accurate for particles with diameter less than 100 µm assembled close together, it was adequate for agglomerate batches generated in this work containing agglomerates in the range of 500-2000 µm.

S.2 Mathematical model for nucleation of spherical agglomerates by the immersion mechanism

This section outlines equations governing the spherical agglomeration process through the immersion mechanism. Most of these equations are derived and discussed in detail in Arjmandi-Tash et al. [31]. In the immersion mechanism of agglomeration, the bridging liquid droplet size is larger than the primary particle size ($D_d > D_{particle}$). This is the case for C65 agglomerates and LFP-C65 co-agglomerates generated in this work. For immersion mechanism based agglomeration, it has been shown that the agglomerate size can be controlled via tuning of the bridging liquid droplet size [45]. According to the equation,

$$D_{Agg} = D_d/\phi_{cp} \quad \text{(S1)}$$

Where D_d is the initial diameter of the bridging liquid droplet and ϕ_{cp} is the critical-packing liquid volume fraction. For consolidated agglomerates, particle packing fraction is higher thus ϕ_{cp} is lower. Whereas for very porous agglomerates, particles are packed loosely resulting in high value of ϕ_{cp}. Similar to Figure 6b, C65 particles exhibit loose packing inside the bridging liquid droplet. Assuming

that only 10 % of the total agglomerate volume is occupied by C65 particles due to bad packing and remaining 90 % is occupied by the bridging liquid,

$$\phi_{cp} = \frac{V_{BL}}{V_{BL} + V_{particles}} = \frac{0.9V_{total}}{0.1V_{total} + 0.9V_{total}} = 0.9 \tag{S2}$$

Based on the solids loading in the continuous phase and wettability properties of the particles, immersion mechanism based agglomeration can be differentiated in two regimes: immersion-rate limited and collision-rate limited. The agglomerate nucleation number *AgNu* can be calculated to determine the regime for a given agglomeration system.

$$AgNu = \frac{Ca\phi_{Pb}}{\lambda} \tag{S3}$$

Ca is a modified capillary number defined by,

$$Ca = \frac{15\mu_d\alpha\left[u(D_p)^2 + u(D_d)^2\right]^{1/2}}{2\Psi\gamma\cos\theta\,\phi_{cp}^2} \tag{S4}$$

And λ is the ratio of the particle size ($D_{particle}$) to the bridging liquid droplet size (D_d),

$$\lambda = \frac{D_{particle}}{D_d} \tag{S5}$$

In Eq. (S4) defining the modified capillary number Ca, μ_d is the viscosity of the bridging liquid. α is the target efficiency,

$$\alpha = \frac{\xi D_p}{2gD_d}\left[u(D_p)^2 + u(D_d)^2\right]^{1/2} \tag{S6}$$

ξ is defined as,

$$\xi = \left[\frac{32}{225}\frac{\left(\rho_p - \rho_L\right)^2 g^2}{\rho_L\mu_L}\right]^{1/3} \tag{S7}$$

Velocity terms $u(D_i)^2$ are defined as,

$$u(D_i)^2 = \left[\frac{(|\rho_i - \rho_L|)^3}{200\rho_L\mu_L(2\rho_i + \rho_L)}\right]^{1/2} D_i^{3/5}\varepsilon^{2/5} \tag{S8}$$

Here, ρ_i's are the densities of particle (ρ_p) and bridging liquid (ρ_d). ρ_L and μ_L is the density and viscosity of the continuous phase respectively. ε is the average energy dissipation rate per unit of suspension mass. For Rushton turbine this is given by [46],

$$\varepsilon = \frac{5.8n^3D^5}{V_T} \tag{S9}$$

Here n is the impeller speed in rad/s, D is the impeller diameter, and V_T is the volume of the tank. In Eq. (S4) defining the modified capillary number Ca, Ψ is the sphericity factor of the primary particles.

For carbon black C65 nanoparticles it is assumed to be 0.8. Interfacial tension between the bridging liquid and the continuous phase is denoted by γ, while θ represents the bridging liquid/solid contact angle at three-phase bridging liquid/continuous phase/solid contact line.

Now the collision rate of particles with the bridging liquid droplet in a turbulent flow can be given by,

$$Q_{coll} = \alpha\left[u(D_p)^2 + u(D_d)^2\right]^{1/2}\phi_{Pb} \tag{S10}$$

As can be observed from Table S1, $AgNu < 0.01$ implying agglomeration in current setup is occurring in collision-rate limited regime. The process is controlled by the collision and arrival of the particles at the bridging liquid droplet surfaces. For this case, the agglomerate size is given by,

$$D_{Agg}(t) = D_d + \frac{D_d}{TBSR}\left(1 - \exp\left(-\frac{2\alpha\left[u(D_p)^2 + u(D_d)^2\right]^{1/2}\phi_{Pb0}TBSR}{D_d}t\right)\right) \tag{S11}$$

Detailed derivation of this equation can be found in Arjmandi-Tash et al. [31]. Here, ϕ_{Pb0} is the initial particle volume fraction in the continuous phase. The timescale for complete immersion of particles inside the bridging liquid droplets in a batch agglomeration system can be calculated by:

$$t_{coll\_bat} = \frac{D_d}{2\alpha\left[u(D_p)^2 + u(D_d)^2\right]^{1/2}\phi_{Pb0}TBSR} Ln\left(\frac{1}{1 - TBSR\frac{(1-\phi_{cp})}{\phi_{cp}}}\right) \tag{S12}$$

At this time agglomerate size reaches its maximum value given by Eq. (S1). To use this equation, value of $TBSR\frac{(1-\phi_{cp})}{\phi_{cp}}$ should be between 0 and 1. When this value is greater than 1, the timescale for complete immersion of particles inside the bridging liquid droplets in a continuous agglomeration system is used instead,

$$t_{coll\_cont} = \frac{D_d(1-\phi_{cp})}{2\alpha\left[u(D_p)^2 + u(D_d)^2\right]^{1/2}\phi_{Pb0}\phi_{cp}} \tag{S13}$$

Diameter of the bridging liquid droplet (D_d) needs to be determined before employing above equations. Here, the correlation derived by Calabrese et al. [47,48] is implemented as it takes into account the effect of viscosity and volume fraction of the dispersed phase. Eq. (S12) has been shown to agree with experimental results for Rushton Turbine [49].

$$D_d = D\left(0.054(1+3\varphi_d)We^{-0.6}\left[1 + 4.42Vi(1-2.5\varphi_d)\left(\frac{D_d}{D}\right)^{0.33}\right]^{0.6}\right) \tag{S14}$$

Where, viscosity number Vi is given by,

$$Vi = \frac{\mu_d nD}{\gamma}\left(\frac{\rho_L}{\rho_D}\right)^{0.5} \tag{S15}$$

Where, φ_d is the dispersed phase volume fraction and We is the Weber number given by,

$$We = \frac{\rho_L n^2 D^3}{\gamma} \tag{S16}$$

Values of different parameters used in these equations are tabulated in Table S1 for C65 agglomeration (corresponding to 3 ml of injected chloroform, TBSR = 9.2). Although carbon black particles are in the nanometer range, particle diameter of 10 nm is used to take into account the incomplete dispersion of C65 particles observed in the continuous phase.

Table S1: Parameter values for C65 agglomeration and LFP-C65 co-agglomeration process.

Parameter	**Symbol**	**C65 agglomeration**
Material/process parameters		
Particle diameter	$D_{particle}\ (m)$	1.00E-08
Dispersed phase viscosity	$\mu_d\ or\ \mu_d^{MDP}\ (Pa.s)$	0.0005
Continuous phase viscosity	$\mu_L\ (Pa.s)$	0.001
Interfacial tension	$\gamma\ (N/m)$	0.022
Three phase contact angle	$\theta\ (°)$	80
Particle density	$\rho_p\ (kg/m^3)$	1900
Dispersed phase density	$\rho_d or\ \rho_d^{MDP}\ (kg/m^3)$	1490
Continuous phase density	$\rho_L\ (kg/m^3)$	1000
Impeller speed	$n\ (rad/s)$	104.7198
Impeller diameter	$D\ (m)$	0.03
Tank volume	$V_T\ (m^3)$	0.0002
Average energy dissipation rate per unit suspension mass	$\varepsilon(m^2/s^3)$	809.2638214
Sphericity factor	$\Psi(-)$	0.8
Critical-packing liquid volume fraction	$\phi_{cp}(-)$	0.9
Initial particle volume fraction in the continuous phase	$\phi_{Pb0}(-)$	0.001051525
True bridging liquid to solids ratio	$TBSR\ (-)$	9.2
Calculated parameters		
Dispersed phase volume fraction	$\varphi_d\ or\ \varphi_d^{MDP}$	0.014778325
Dispersed phase droplet diameter	$D_d\ or\ D_d^{MDP}(m)$	5.68542E-06
Particle-continuous phase relative velocity	$u(D_p)\ (m/s)$	0.006360104
Dispersed phase droplet-continuous phase relative velocity	$u(D_d)\ (m/s)$	0.126162771
	$\xi(1/s)$	222.8272036
Target efficiency	$\alpha\ (-)$	0.002525991
Agglomerate diameter	$D_{Agg}(m)$	6.31713E-06
Timescales		
Timescale for complete immersion of particles inside the dispersed phase droplet limited by immersion rate	$t_{imm}\ (s)$	0.00027203
Timescale for complete immersion of particles inside the dispersed phase droplet limited by	$t_{coll\_cont}\ (s)$	0.94136146

collision rate for continuous agglomeration system		
Timescale for complete immersion of particles inside the dispersed phase droplet limited by collision rate for batch agglomeration system	$t_{coll\_bat}\ (s)$	33.93010618
Dimensionless parameters		
Modified capillary number	$Ca\ (-)$	0.000483368
Ratio of particle size to dispersed phase droplet size	$\lambda(-)$	1.76E-03
Agglomerate nucleation number	$AgNu\ (-)$	2.89E-04

As can be observed from Table S1, the agglomeration nucleation number $AgNu \ll 1$ implying that the immersion is limited by the collision rate. The immersion timescale values are less than 1 min. Since the agglomerates are obtained at more than 10 min, the agglomerate size is assumed to reach its maximum value given by Eq. (S1).

This agglomeration nucleation model has limited applicability to spherical agglomeration of carbon black particles. Since to truly achieve agglomerates comparable to the initial bridging liquid droplet size though the immersion mechanism, multiple requirements need to be satisfied. The particles in the continuous phase need to be dispersed well to ensure agglomeration occurs through the immersion mechanism rather than the distribution mechanism Figure 1. This implies that the bridging liquid droplet diameter needs to be larger than the largest dispersed aggregate in the continuous phase ($D_d > D_{Particle}$). Additionally, coalescence of the bridging liquid droplets and agglomerates need to be avoided at all stages of the agglomeration process. Finally, careful filtration and drying of the formed agglomerates is required to avoid coalescence during the filtration and drying stage. In this work, ultra-sonication based pre-processing is performed to disperse the particles in the continuous phase. Filtration is performed slowly in multiple stages involving sieves and filter papers. Slow overnight drying is performed to avoid movement of the particles inside the agglomerates during drying. Still some coalescence is expected and agglomerate size is expected to be larger than the one predicted through this model.

S.3 Effect of agglomeration time

Optical microscope images of LFP-C65 co-agglomerate batches obtained at different agglomeration times are shown here.

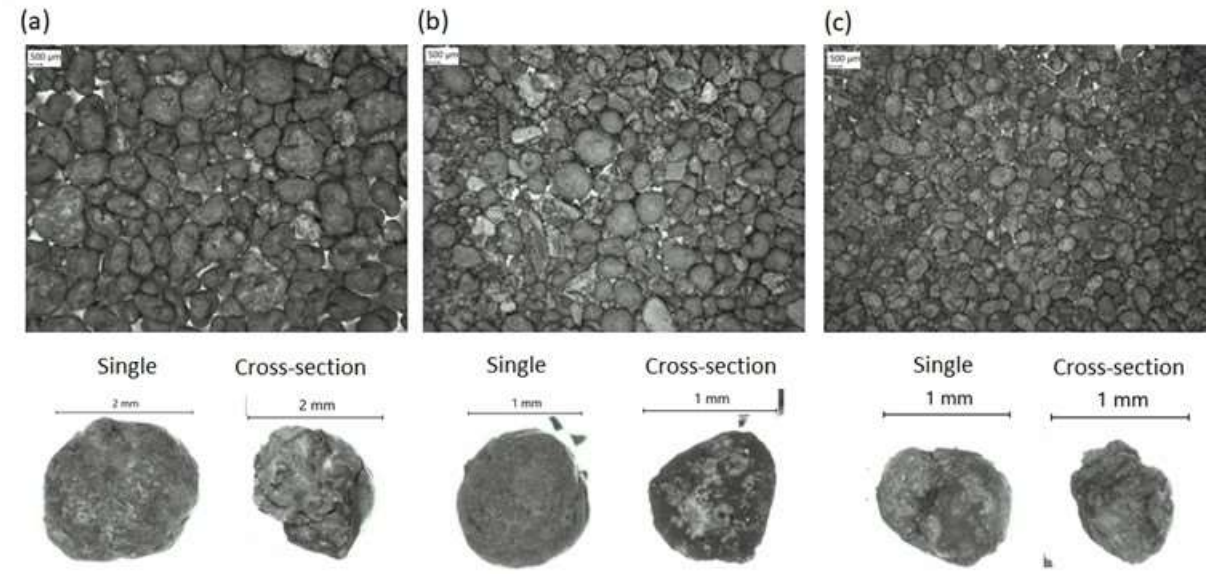

Figure S7: Generated LFP (grey)-C65 (black) co-agglomerates, single co-agglomerate, and co-agglomerate cross-section for (a) agglomeration time = 10 min, (b) agglomeration time = 20 min, and (c) agglomeration time = 40 min.

S.4 Effect of solids loading

Optical microscope images of LFP-C65 co-agglomerate batches obtained at different solids loadings are shown here.

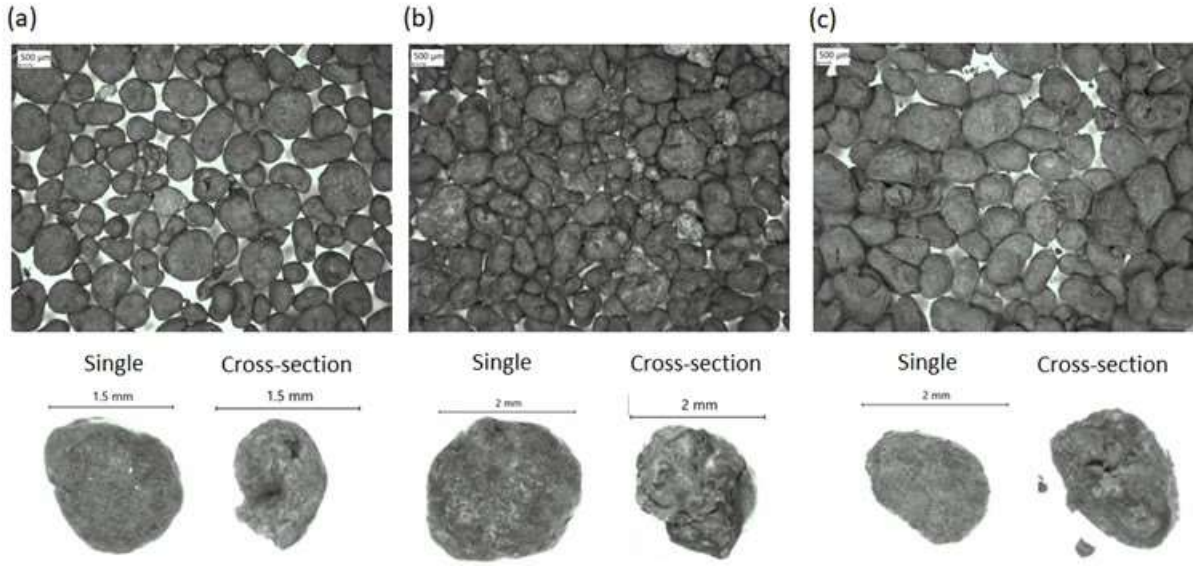

Figure S8: Generated LFP (grey)-C65 (black) co-agglomerates, single co-agglomerate, and co-agglomerate cross-section for (a) solids loading = 0.5 %, (b) solids loading = 1.0 %, and (c) solids loading = 2.0 %.

S.5 Effect of impeller speed

Optical microscope images of LFP-C65 co-agglomerate batches obtained at different impeller speeds are shown here.

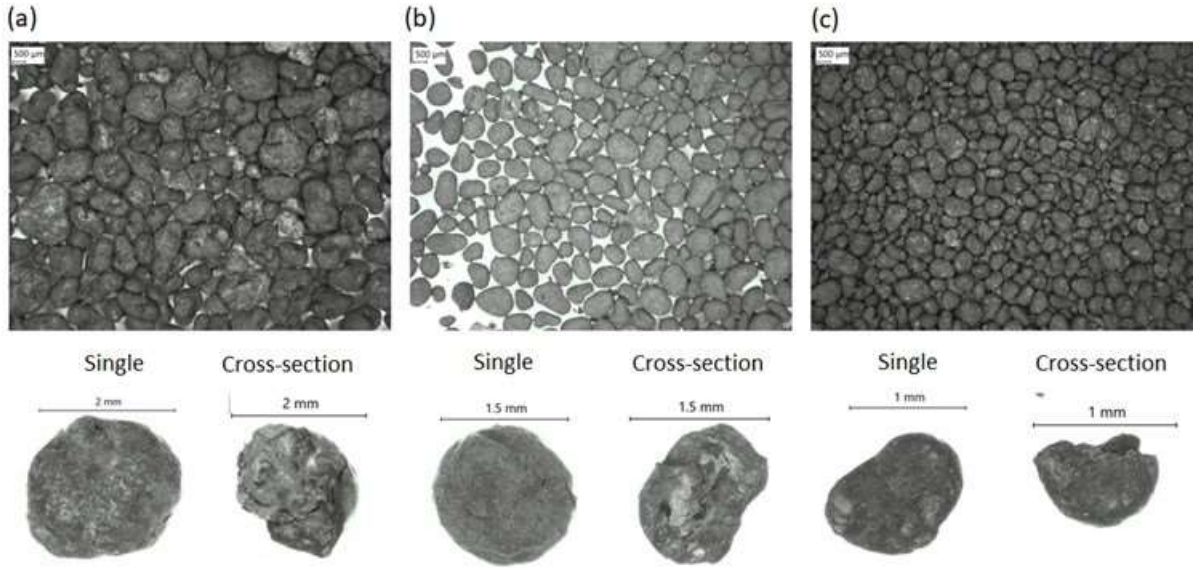

Figure S9: Generated LFP (grey)-C65 (black) co-agglomerates, single co-agglomerate, and co-agglomerate cross-section for (a) impeller speed = 1000 RPM, (b) impeller speed = 1250 RPM, and (c) impeller speed = 1500 RPM.